J. Fluid Mech. (2020), *vol*. 902, A20. © The Author(s), 2020.
Published by Cambridge University Press
doi:10.1017/jfm.2020.488

Direct numerical simulation of a non-equilibrium three-dimensional turbulent boundary layer over a flat plate

Hiroyuki Abe†

Japan Aerospace Exploration Agency, Tokyo 182-8522, Japan

(Received 26 September 2019; revised 20 May 2020; accepted 14 June 2020)

Direct numerical simulations (DNS) are used to examine a spatially developing non-equilibrium three-dimensional turbulent boundary layer (3DTBL) over a flat plate. The present flow is a 'shear-driven' 3DTBL owing to a sudden imposition of a surface spanwise velocity W_S. Particular attention is given to the effects of cross-flow and Reynolds number. In the DNS, three values of the inlet momentum thickness Reynolds number, $Re_{\theta_0} = 300$, 600 and 900, are used with several values of W_S. The present largest W_S is twice the free-stream velocity U_0, comparable to the maximum value of the spinning cylinder experiment by Lohmann (*Trans. ASME* I*: J. Fluids Engng*, vol. 98, 1976, pp. 354–363). After imposing W_S, the mean streamwise vorticity $\overline{\Omega}_x$ increasingly propagates away from the wall where there is close relationship between a deficit of mean streamwise velocity and inviscid skewing (i.e. three-dimensionality). At a downstream station of a 3DTBL, near-plateaus appear in the skin friction coefficients where the magnitudes depend intrinsically on W_S. The approach to the collateral state is, however, slow for mean streamwise velocity $\overline{U}$ where the Reynolds shear stress $\overline{uv}$ extracts energy from the mean flow inefficiently. As the Reynolds number increases, the mean velocity magnitude Q_r tends to show the log law but with a larger von Kármán constant than in a two-dimensional turbulent boundary layer. Instantaneously, toppling u structures dominate owing to cross-flow and become more prominent with increasing Re. Statistically, the latter spanwise length scale increases linearly with respect to y below $y/\delta_{99} = 0.2$, which indicates that cross-flow yields a self-similar behaviour.

Key words: turbulence simulation, turbulent boundary layers

1. Introduction

Three-dimensional turbulent boundary layers (3DTBLs) are often encountered in engineering and aeronautical applications, which are classified either by a skewed turbulent boundary layer (TBL) caused by transverse strain (referred to as 'Prandtl's first kind of secondary flow'), e.g. a flow over a swept wing, or by a stress-induced secondary flow (referred to as 'Prandtl's second kind of secondary flow'), e.g. a wing–body junction flow (see Bradshaw 1987). Detailed data for 3DTBLs, however, may not be sufficient

† Email address for correspondence: habe@chofu.jaxa.jp

from direct numerical simulation (DNS), especially with respect to the Reynolds-number dependence. DNS resolves all the essential motions of turbulence. The resulting data thus have potential not only for better understanding the underlying physics of turbulence but also for developing turbulence models.

One of the challenging issues regarding 3DTBLs is a non-equilibrium 3DTBL due to a sudden imposition of a transverse strain to a two-dimensional turbulent boundary layer (2DTBL). Van den Berg *et al*. (1975) and Bradshaw & Pontikos (1985) carried out infinite-swept-wing experiments (the former work involves separation). Bradshaw & Pontikos (1985) reported a significant decrease in the magnitude of the Reynolds shear stress $\overline{uv}$, compared with an equivalent 2DTBL. (Note that u, v and w denote the streamwise, wall-normal and spanwise velocity fluctuations, respectively; u_1, u_2 and u_3 are also used interchangeably with u, v and w throughout the paper; upper case refers to an instantaneous velocity; and an overbar denotes averaging in both space and time.) They also noted that the direction of the Reynolds stress lags behind that of the mean strain rate. These are representative features in a non-equilibrium 3DTBL, which have also been examined via a DNS.

A seminal DNS work was undertaken by Moin *et al*. (1990) in a turbulent channel flow. In their simulation, they suddenly imposed a spanwise mean pressure gradient to an initially two-dimensional (2-D) channel flow at the Kármán number (or equivalently, the friction Reynolds number) $Re_\tau(\equiv h^+) = U_\tau h/\nu = 180$. This flow is thus a temporally developing non-equilibrium 3DTBL. Here, Re_τ represents the ratio of the half-width of the channel h and the viscous length scale ν/U_τ (where ν is the viscosity and $U_\tau \equiv (\tau_w/\rho)^{1/2}$ is the friction velocity, with τ_w the wall shear stress and ρ the density of the fluid; the superscript $^+$ denotes normalization by wall units). It was noted that the Reynolds stress lags behind the mean strain rate; the structure parameter $a_1 \equiv \tau/q^2$ is smaller than the value of 0.15 in the 2DTBL due to the decrease in the Reynolds shear stress $\overline{uv}$, where $\tau \equiv (\overline{vw}^2 + \overline{uv}^2)^{1/2}$ and $q^2 \equiv 2k = \overline{u_i u_i}$ denote the total shear stress and twice the turbulent kinetic energy, respectively. The latter result implies that the non-equilibrium 3DTBL is less efficient for extracting energy from mean flow than the 2DTBL. Sendstad & Moin (1992) subsequently argued that the reduction in a_1 is due not to the rotation of the stress vector or the strain vector, but to structural changes of three-dimensionality since the total shear stress τ and the turbulent kinetic energy k are invariant with respect to the coordinate system. On the other hand, Coleman, Kim & Le (1996) performed a 'shear-driven' DNS in a turbulent channel flow for $Re_\tau = 180$ owing to the surface spanwise velocity (the latter magnitude being half the centreline velocity). Like Moin *et al*. (1990), Coleman *et al*. (1996) observed a decrease in magnitude of a_1 and a lag in the direction between the Reynolds shear stress and the strain rate in their simulation. They also noted that the most significant effect of shear-driven three-dimensionality is a modification of the interaction between near-wall streaks and quasi-streamwise vortices, which can be attributed to the reduction in $\overline{uv}$ and hence a_1.

Subsequently, Coleman, Kim & Spalart (2000) carried out a DNS of a time-developing strained channel flow for $Re_\tau = 180$ as an idealization of pressure-driven TBLs. They found that the impact of the adverse pressure gradient (APG) on the outer-layer structure is more pronounced than that of the mean three-dimensionality, i.e. the structure parameter a_1 experiences a much larger decrease when the APG strain is present. They also noted that the temporal evolution of the Reynolds shear stress is significantly affected by the changes to the velocity–pressure gradient correlation (VPG) term, which is primarily responsible for the lag in direction between the mean shear and the Reynolds shear stress. The recent 3DTBL DNS of Lozano-Durán *et al*. (2020) in a turbulent channel flow with a sudden

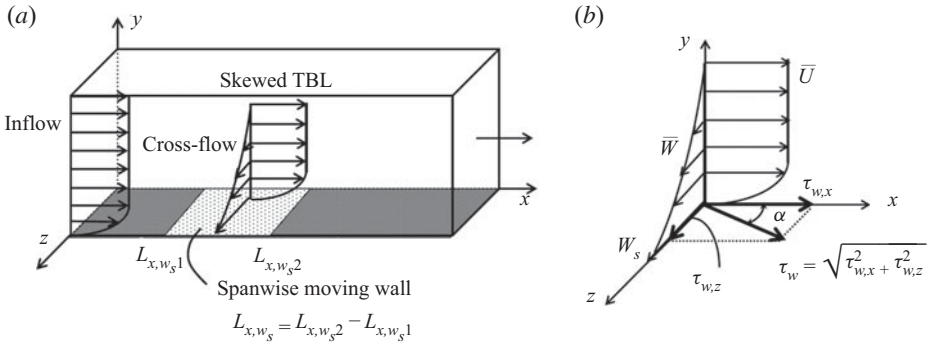

FIGURE 1. Schematic diagrams: (*a*) computational domain; and (*b*) mean velocity and shear-stress components in a 3DTBL.

imposition of a spanwise mean pressure gradient is of note. They performed simulations at $Re_\tau = 500$ and 1000, and noted that the flow regimes and scaling properties of the Reynolds stress are consistent with a model comprising momentum-carrying eddies with sizes and time scales proportional to their distance to the wall.

In the present study, we work on a 'spatially developing' shear-driven non-equilibrium 3DTBL via a DNS. The present DNS set-up has been established by referring to the spinning cylinder experiments of Bissonnette & Mellor (1974), Lohmann (1976), Driver & Hebbar (1987) and Driver & Johnston (1990) – see figure 1(*a*) where the computational domain is shown; unlike in the experiments, the present flow is free of any curvature effect. Since the shear-driven 3DTBL does not involve the spanwise pressure gradient, this flow isolates the effect of pressure gradient. In the present simulation, a zero-pressure-gradient (ZPG) TBL over a flat plate is subjected to a sudden surface spanwise velocity W_S, the latter yielding the secondary Reynolds shear stress $\overline{vw}$ and thus cross-flow (see § 3). The sudden imposition of W_S is important for better understanding a non-equilibrium 3DTBL and also the approach to the equilibrium state.

In the current 'shear-driven' DNS, the mean streamwise vorticity $\overline{\Omega}_x$ is therefore generated at the wall and diffuses into the outer region, whereas in the 'pressure-driven' DNS (Schlatter & Brandt 2010), three-dimensionality is introduced by prescribing varying $\overline{U}$ and $\overline{W}$ at the upper boundary (see also McLean (2013), who explains the difference in the mean velocity profile between shear-driven and pressure-driven flows). The transport equation of $\overline{\Omega}_x$ may be expressed as follows:

$$\frac{\mathrm{D}\overline{\Omega}_x}{\mathrm{D}t} = \overline{\Omega}_x\frac{\partial\overline{U}}{\partial x} + \overline{\Omega}_y\frac{\partial\overline{U}}{\partial y} + \overline{\Omega}_z\frac{\partial\overline{U}}{\partial z} + \left(\frac{\partial^2}{\partial z^2} - \frac{\partial^2}{\partial y^2}\right)\overline{vw} + \frac{\partial^2}{\partial y\partial z}(\overline{vv} - \overline{ww}) + \nu\nabla^2\overline{\Omega}_x \tag{1.1}$$

(see Bradshaw 1987), where x, y and z denote the streamwise, wall-normal and spanwise directions, respectively; t refers to time; x_1, x_2 and x_3 are also used interchangeably with x, y and z throughout the paper. In the present flow, the streamwise variation of $\overline{\Omega}_x$ may be expressed as

$$\overline{U}\frac{\partial\overline{\Omega}_x}{\partial x} = \overline{\Omega}_z\frac{\partial\overline{W}}{\partial x}, \tag{1.2}$$

since $\partial\overline{U}/\partial z = \partial\overline{W}/\partial x$ due to the irrotational condition, i.e. the mean wall-normal vorticity $\overline{\Omega}_y = 0$ (see Bradshaw 1987; Sendstad & Moin 1992; Coleman *et al.* 2000). Here, $\partial\overline{W}/\partial x$ is responsible for inviscid skewing (i.e. three-dimensionality) of the mean spanwise vorticity $\overline{\Omega}_z$.

A schematic diagram of velocity profiles and wall shear-stress components in a shear-driven 3DTBL is shown in figure 1(*b*). As observed in the experiments of Bissonnette & Mellor (1974) and Lohmann (1976), when the flow enters into the region imposing W_S, i.e. L_{x,W_S} (defined in § 2.1), the flow near a wall first approaches the wall shear-stress direction (i.e. α), whereas the outer flow is three-dimensional (3-D) and the Reynolds shear-stress angle lags behind the mean velocity gradient direction. The approach to the collateral state thus depends intrinsically on L_{x,W_S}. In this context, Lohmann (1976) reported in his spinning cylinder experiment that the transverse mean velocity and wall shear-stress component attain an asymptotic state in the streamwise distance of approximately $10\delta_0$ (where δ_0 denotes the boundary layer thickness at the reference station). This point will be examined further in § 3.1 with varying L_{x,W_S}.

When L_{x,W_S} is sufficiently long, the mean flow will eventually become 2-D across the boundary layer at a downstream station. The latter is called a 'collateral' boundary layer in which the mean flow direction coincides with the angle $\tan^{-1}(W_S/U_0)$ (where U_0 denotes the reference free-stream velocity) – see also the seminal experimental work on a skewed TBL over a spinning body of Furuya, Nakamura & Kawachi (1966). The mean velocity magnitude Q_r then follows the 'law of the wall', *viz.*

$$Q_r^+ \equiv \frac{Q_r}{U_\tau} = \frac{1}{\kappa}\ln(y^+) + A, \tag{1.3}$$

where κ and A denote von Kármán constant and an additive constant, respectively; and U_τ denotes the friction velocity, defined in (3.1). Also, given the collateral state, the logarithmic law of mean streamwise velocity can be written as

$$\frac{\overline{U}}{U_{\tau,x}} = \frac{1}{\kappa_x}\ln\left(\frac{U_{\tau,x}y}{\nu}\right) + A_x, \tag{1.4}$$

with $U_{\tau,x} = \mu(\partial\overline{U}/\partial y)|_w$, $\kappa_x = \kappa/\sqrt{\cos\alpha}$ and $A_x = A\sqrt{\cos\alpha} - \ln(\cos\alpha)/2\kappa_x$. Indeed, relations (1.3) and (1.4) hold unambiguously in the recent DNS of a turbulent separation bubble with sweep by Coleman, Rumsey & Spalart (2019), who provide cross-flow by imposing spanwise velocity at the free stream (this flow is thus a pressure-driven 3DTBL). They also noted that the non-zero spanwise component of mean velocity in the collateral boundary layer is solely an artefact of the orientation of the coordinate system. The approach to the collateral state will be discussed in § 3.1, with the use of (1.3) and (1.4).

In a spatially developing non-equilibrium 3DTBL, inviscid skewing has a close relationship with the deficit of streamwise mean velocity, *viz.*

$$\frac{\partial\overline{W}}{\partial x} = -\overline{U}\frac{\partial\alpha}{\partial x} \tag{1.5}$$

and

$$\frac{\partial\overline{U}}{\partial x} = -\overline{U}\frac{\partial\alpha}{\partial z}. \tag{1.6}$$

Relations (1.5) and (1.6) are obtained using the continuity equation and irrotationality condition, respectively (see Johnston 1960). Note that when the skewing is completed

(i.e. the collateral state is established), both (1.5) and (1.6) become negligibly small. The relationship between (1.5) and (1.6) will be discussed in § 3.2.

In the present flow, the seminal numerical simulation was done by Kannepalli & Piomelli (2000) with the use of a wall-resolved large-eddy simulation (LES). They examined the effect of cross-flow for two different magnitudes of $W_S/U_0 = 0.3$ and 1.0, where $Re_\theta \approx 1100$ in their 3DTBL. Here, $Re_\theta (\equiv U_\infty \theta/\nu)$ denotes the Reynolds number based on the local free-stream velocity U_∞ and the local momentum thickness, *viz.*

$$\theta \equiv \int_0^\infty \frac{\overline{U}}{U_\infty}\left(1 - \frac{\overline{U}}{U_\infty}\right) \mathrm{d}y. \tag{1.7}$$

The latter magnitude increases on moving downstream (see figure 13*b*). Also used in this paper is the Reynolds number $Re_{\theta_0} \equiv U_0\theta_0/\nu$ based on the inlet momentum thickness θ_0. They observed the above-mentioned features in a non-equilibrium 3DTBL, and noted that the reduction in a_1 appears to be associated with the response of the turbulence to the perturbation, rather than 3-D effects *per se*. They also found that the integral of the mean spanwise velocity (i.e. spanwise momentum thickness),

$$\theta_z \equiv \int_0^\infty \overline{W}\,\mathrm{d}y, \tag{1.8}$$

normalized by the surface spanwise velocity W_s, is proportional to a half-power law, i.e. $\theta_z/W_s \sim x^{1/2}$, as in the internal boundary layer (this refers to a new boundary layer created inside the existing boundary layer due to a change of a surface condition) by Antonia & Luxton (1971), who carried out an experiment in a TBL with a sudden change of surface condition from a smooth wall to a rough wall. They demonstrated that a half-power-law dependence in θ_z/W_s is intrinsically associated with the Stokes layer in which $\theta_z \sim t^{1/2}$. Kannepalli & Piomelli (2000) also discussed a possible scaling law of the spanwise skin friction coefficient $C_{f,z}$ (defined in § 3.1) for $W_S/U_0 = 1$ by comparing with the experimental data of Driver & Johnston (1990) ($Re_\theta = 6000$ in a trailing edge of the spinning cylinder). They used a normalization by $U_e W_s/2\rho$ (see relation (4.1)). This mixed scaling was shown to be successful for a small magnitude of W_S (i.e. $W_S/U_0 \leq 1$). However, it is not clear if this scaling law may hold for a larger value of W_S than $W_S/U_0 = 1$. Also, while L_{x,W_s} in their simulations is within the condition of Lohmann (1976) on the equilibrium state, their streamwise skin friction coefficient does not exhibit a plateau in a 3DTBL (see figure 8 of their paper). This observation indicates that the approach to the collateral boundary layer is likely to be slow in the present flow. This will be pursued further in the present study.

Here, we carry out a series of DNS in a spatially developing shear-driven non-equilibrium 3DTBL over a flat plate. Some preliminary results have been presented by Abe (2018). The present inlet momentum thickness Reynolds number is equal to $Re_{\theta 0} = 300$, 600 and 900. The largest $Re_{\theta 0}$ case covers the Reynolds-number range of the LES work by Kannepalli & Piomelli (2000) (see table 2), this latter work being compared in the present study. Also made are comparisons with the spinning cylinder experiments of Lohmann (1976) and Driver & Hebbar (1987) – their Reynolds numbers in a trailing edge of the spinning cylinder are for $Re_\theta \approx 2420$ and 6000, respectively – and with the particle image velocimetry (PIV) measurement for a 3DTBL (generated by a spanwise translating belt) over a flat plate by Kiesow & Plesniak (2003) – the Reynolds number is $Re_\theta = 1450$ in their PIV measurement. Several values of W_S/U_0 are used in the present

DNS. The largest $W_S/U_0(= 2.0)$ is comparable to the value (=2.2) of the spinning cylinder experiment by Lohmann (1976). Particular attention is given to the effects of cross-flow and Reynolds number in a shear-driven non-equilibrium 3DTBL. In particular, we discuss how the 2DTBL is turned (skewed) by an impulsive surface spanwise velocity and how the resulting skin friction coefficients vary in a non-equilibrium 3DTBL. The latter behaviour will be examined by decomposing the skin friction coefficients into the mean and turbulent parts using the relation of Renard & Deck (2016) (i.e. relation (4.2)) established in a 2DTBL based on the energy balance for the mean velocity. This relation is analogous to the FIK identity (Fukagata, Iwamoto & Kasagi 2002) derived on the basis of the mean momentum balance. The results will be compared with the global energy balance analysis in a turbulent channel flow by Abe & Antonia (2016) and Wei (2018), and discussed in terms of the amount of energy extracted from the mean flow in a 3DTBL due to the work done by the Reynolds shear stress.

We also examine how the mean velocity and the Reynolds stress are altered in a non-equilibrium 3DTBL by comparing with those of a 2DTBL and an equilibrium 3DTBL (Spalart 1989; Littell & Eaton 1994; Wu & Squires 1997; Kang, Choi & Yoo 1998). Experimentally, there is evidence that the slope of the logarithmic mean velocity profile is decreased (i.e. the von Kármán constant is thus increased) in non-equilibrium 3DTBLs (Bissonnette & Mellor 1974; Pierce & McAllister 1983; Moin *et al*. 1990). This latter point will be discussed by focusing not only on the overlap scaling of mean velocity (*viz*. law of the wall) but also on that of the energy dissipation rate. We also examine turbulence structures in a non-equilibrium 3DTBL in light of the toppling structures hypothesized by Bradshaw & Pontikos (1985), and discuss the extent to which the interaction between the inner and outer regions varies there, since Kevin, Monty & Hutchins (2019) recently observed, in their 3DTBL experiment on a ribbed surface, that the inner–outer relationship decreases above the angled ribs, as the turbulence is leaning sideways.

Focus is also put on the most energetic spanwise scales of velocity fluctuations, as was done by Jiménez & Hoyas (2008), Hwang (2015) and Abe, Antonia & Toh (2018) in a turbulent channel flow. In particular, we investigate if the spanwise length scales increase linearly with distance from the wall in the present 3DTBL, and follow the attached-eddy hypothesis (Townsend 1976) given that Lozano-Durán *et al*. (2020) recently reported a self-similar response of a non-equilibrium 3DTBL in their 3-D channel with a sudden imposition of mean spanwise pressure gradient. In the recovery region, attention is given to what extent the present 3DTBL recovers to a ZPG TBL state after turning off W_S in light of the seminal work of Antonia & Luxton (1971) on the sudden change of surface condition in a TBL. We hope that the present DNS analysis provides further insight into a non-equilibrium 3DTBL.

This paper is organized as follows. Section 2 describes the DNS set-up. The present inflow is a 2-D ZPG TBL, which is subjected to a sudden imposition of the surface spanwise velocity W_S, as in the spinning cylinder experiments (e.g. Bissonnette & Mellor 1974; Lohmann 1976; Driver & Hebbar 1987; Driver & Johnston 1990). It is thus initially a non-equilibrium 3DTBL, which ends up by approaching an equilibrium 3DTBL downstream. In § 3, we explain the basic features of a shear-driven non-equilibrium 3DTBL for $Re_{\theta_0} = 300$ with $W_S/U_0 = 1$. Section 3.1 discusses the value of L_{x,W_S} (i.e. the streamwise extent of imposing W_S) and the approach to the collateral boundary layer. In § 3.2, we examine the relationship between the mean streamwise velocity deficit and inviscid skewing (i.e. (1.5) and (1.6)). Section 3.3 explains how the mean velocity and Reynolds stress vary on moving downstream in the present 3DTBL.

In § 4, we investigate the effect of cross-flow in a non-equilibrium 3DTBL for $Re_{\theta 0} = 300$ with varying W_S (i.e. $W_S/U_0 = 0$, 0.1, 0.5, 1, 1.5 and 2). Section 4.1 examines the effect of cross-flow on the skin friction coefficients. In particular, we perform an analysis using the relation of Renard & Deck (2016) on the mean energy balance to gain further insight into the behaviour of the skin friction coefficients in a 3DTBL. In § 4.2, the variation of near-wall turbulence structures (i.e. streaks and quasi-streamwise vortices) is discussed. Section 4.3 examines the near-wall Reynolds stresses and the energy redistribution. In § 5, we investigate the effect of Reynolds number in both 3DTBL and recovery regions for three Reynolds numbers (i.e. $Re_{\theta_0} = 300$, 600 and 900) with intermediate and large magnitudes of cross-flow (i.e. $W_S/U_0 = 1$ and 2).

Section 5.1 discusses the Re dependence of the momentum thicknesses and skin friction coefficients. In § 5.2, attention is given to the 'law of the wall' in a non-equilibrium 3DTBL with focus on the mean velocity magnitude and the energy dissipation rate. Section 5.3 discusses asymmetric turbulence structures observed in a non-equilibrium 3DTBL. In particular, we examine the interaction between the inner and outer regions and the most energetic spanwise scales of velocity fluctuations. Section 5.4 examines the reduced magnitude of the primary Reynolds shear stress $-\overline{uv}$ and the implication for turbulence modelling. In § 5.5, we investigate the recovery to a ZPG TBL. Conclusions are given in § 6.

2. DNS set-up

2.1. *Computational domain*

A schematic diagram of the present computational domain is shown in figure 1(*a*). The inflow is a spatially developing 2-D ZPG TBL over a flat plate (this point will be detailed in § 2.3). After the inlet, the present TBL develops under the ZPG in the region $0 \leq x \leq L_{Ws1}$. The flow is then subjected to a sudden imposition of the surface spanwise velocity W_S in the region $L_{Ws1} \leq x \leq L_{Ws2}$ (this latter region is referred to as the '3DTBL region' in this paper). The streamwise extent of imposing W_S, i.e. $L_{x,W_S} = L_{Ws2} - L_{Ws1}$, will be examined in § 3.1 in light of Lohmann's (1976) condition on the near-equilibrium 3DTBL state. Note that different values of L_{x,W_S} are used for $Re_{\theta_0} = 300$ and for $Re_{\theta_0} = 600$ and 900 (see table 1) since a longer L_{x,W_S} is required for a lower L_{x,W_S} to obtain a near-plateau in both the streamwise and spanwise skin friction coefficients (see §§ 3–5). At $x = L_{Ws2}$, W_S is turned off. There is again a sudden change of the surface condition there. The present flow recovers to a ZPG TBL in the region $L_{Ws2} \leq x \leq L_x$ (referred to as the 'recovery region' in this paper).

2.2. *Numerical methodology*

Numerical methodology is briefly as follows. The current DNS code has been developed based on a DNS code for a TBL with separation and reattachment by Abe (2017). A fractional step method is used with semi-implicit time advancement. The Crank–Nicolson method is used for the viscous terms in the y direction, and the third-order Runge–Kutta method is used for the other terms. A finite difference method is used as a spatial discretization. A fourth-order central scheme (Morinishi *et al*. 1998) is used in the x and z directions, whilst a second-order central scheme is used in the y direction.

Re_{θ_0}	300	600	900
W_S/U_0	0, 0.1, 0.5, 1.0, 1.5, 2.0	1.0, 2.0	1.0, 2.0
L_{x,W_S}	$100\theta_0$, $200\theta_0$, $300\theta_0$	$100\theta_0$	$100\theta_0$
$L_x \times L_y \times L_z$		$400\theta_0 \times 80\theta_0 \times 160\theta_0$	
$L_x \times L_y \times L_z$	$24.1\delta_{out} \times 4.8\delta_{out} \times 9.6\delta_{out}$	$25.6\delta_{out} \times 5.1\delta_{out} \times 10.2\delta_{out}$	$27.6\delta_{out} \times 5.5\delta_{out} \times 11.0\delta_{out}$
$N_x \times N_y \times N_z$	$512 \times 160 \times 512$	$1024 \times 320 \times 1024$	$2048 \times 480 \times 1536$
Δx_0^+, Δy_0^+, Δz_0^+	12.4, 0.15–22.3, 4.96	11.5, 0.14–21.2, 4.59	8.24, 0.13–20.4, 4.40
TU_0/θ_0	5500	4125	4308
$TU_{\tau,0}^2/\nu$	9327	11 968	16 499

TABLE 1. Domain size, grid points, spatial resolution and sampling time period. Note that δ_{out} denotes the outlet 99% boundary layer thickness.

As for the boundary condition for W at the wall ($y = 0$), a slip boundary condition (i.e. $W = W_S$) is used in the 3DTBL region (i.e. $L_{W_S1} \leq x \leq L_{W_S2}$), whereas a no-slip boundary condition is used in the other x locations. For U and V at the wall, a no-slip boundary condition is used across the x stations. On the other hand, we impose the following boundary conditions at the upper boundary:

$$\frac{\partial U}{\partial y} = 0, \quad V = U_0 \overline{\frac{\partial \delta_2}{\partial x}}, \quad \frac{\partial W}{\partial y} = 0, \tag{2.1a–c}$$

which are the same ones as for a ZPG TBL by Lund, Wu & Squires (1998). Note that (2.1*b*) (i.e. the wall-normal velocity at the upper boundary) consists of the product of U_0 and $\partial\delta_2/\partial x$ (i.e. the gradient of the displacement thickness at each x station) averaged over the x direction. In the z direction, a periodic boundary condition is used; the spatial averaging for mean and turbulence statistics has been made for this direction. For the outlet, a convective boundary condition is used.

2.3. *Inflow 2DTBL simulation*

The present inflow is a spatially developing 2-D ZPG TBL over a flat plate, which is generated by the rescaling–recycling method (Lund *et al*. 1998) with a spanwise constant shift (Spalart, Strelets & Travin 2006). This simulation has been time-advanced simultaneously with the shear-driven 3DTBL DNS, i.e. the ZPG data at a target Re_θ are provided as the inlet data of a shear-driven 3DTBL DNS. In the inflow simulations, the domain size used for $Re_{\theta_0} = 300$ and 600 is $L_x \times L_y \times L_z = 400\theta_0 \times 80\theta_0 \times 160\theta_0$ where the inlet momentum thickness Reynolds number is set to 300 and 600. On the other hand, the domain size used for $Re_{\theta_0} = 900$ is $L_x \times L_y \times L_z = 1200\theta_0 \times 240\theta_0 \times 480\theta_0$ where the inlet momentum thickness Reynolds number is set to 300. Referring to the seminal DNS by Kong, Choi & Lee (2000), the recycling location has been set to approximately $100\theta_0$ for all the inflow simulations. The validation of the inflow simulation has been presented in Abe (2017). Overall agreement with the existing DNS in a ZPG TBL (Spalart 1988; Simens *et al*. 2009; Wu & Moin 2009; Schlatter & Örlü 2010) is satisfactory (see § 2 of

	$x/\theta_0 = 175$	$x/\theta_0 = 300$
	$W_S/U_0 = 1,\ 2$	$W_S/U_0 = 1,\ 2$
$Re_{\theta_0} = 300$	$Re_\theta = 419,\ 428$	$Re_\theta = 510,\ 535$
$Re_{\theta_0} = 600$	$Re_\theta = 831,\ 852$	$Re_\theta = 993,\ 1033$
$Re_{\theta_0} = 900$	$Re_\theta = 1216,\ 1255$	$Re_\theta = 1431,\ 1495$

TABLE 2. The momentum thickness Reynolds number Re_θ in the 3DTBL ($x/\theta_0 = 175$) and recovery ($x/\theta_0 = 300$) regions. The values tabulated have been obtained with $L_{x,W_S} = 100\theta_0$.

Abe 2017). In the following sections, statistics and turbulence structures for a 2DTBL will be compared with those for a 3DTBL.

2.4. *Flow parameters for the shear-driven 3DTBL DNS*

The computational domain size ($L_x \times L_y \times L_z$), number of grid points ($N_x \times N_y \times N_z$), spatial resolution at the inlet ($\Delta x_0, \Delta y_0, \Delta z_0$) and sampling time period (T) for the shear-driven 3DTBL simulations are given in table 1. The present streamwise domain size (i.e. $L_x/\theta_0 = 400$ or, equivalently, $48\delta_0$) is comparable with $L_x/\theta_0 \approx 350$ (note that this latter domain size does not involve a buffer region of a fringe) of Kannepalli & Piomelli (2000), whereas the spanwise domain size (i.e. $L_z/\theta_0 = 160$ or, equivalently, $19\delta_0$) is a factor of 4 larger than in Kannepalli & Piomelli (2000) – a small spanwise domain (i.e. $L_z/\theta_0 \approx 40$ or, equivalently, $5\delta_0$) is used in their work. Once the velocity field reaches the fully developed and statistically steady state (i.e. time-independent profiles of the skin friction coefficients), the Navier–Stokes equations are integrated further in time to obtain mean flow and turbulence statistics (we have also checked one-point statistics for the first sampling time period (0–$T/2$) and those for the second sampling time period ($T/2$–T) and confirmed that the difference is negligibly small).

In the present study, we examine the effects of cross-flow and Reynolds number in a shear-driven 3DTBL. The former effect is examined for $Re_{\theta_0} = 300$ with varying W_S/U_0 ($= 0$, 0.1, 0.5, 1, 1.5 and 2). On the other hand, the latter effect is investigated for three values of Re_{θ_0} ($= 300$, 600 and 900) with two different magnitudes of W_S/U_0 ($= 1$ and 2). The three values of the inlet momentum thickness Reynolds number, $Re_{\theta_0} = 300$, 600 and 900, correspond to those of the friction Reynolds number, $Re_{\tau_0} \equiv U_{\tau_0}\delta_{99_0}/\nu = 140$, 250 and 350, respectively (here U_{τ_0} and δ_{99_0} denote the inlet friction velocity and 99 % boundary layer thickness, respectively). In the present flow, the momentum thickness Reynolds number increases with increasing x (see figure 13*a*). Also shown in table 2 is the momentum thickness Reynolds number Re_θ in the 3DTBL ($x/\theta_0 = 175$) and recovery ($x/\theta_0 = 300$) regions. At $x/\theta_0 = 175$, the largest Re_θ ($= 1255$) is attained for $Re_{\theta_0} = 900$ with $W_S/U_0 = 2$, the latter magnitude of Re_θ being close to that (i.e. $Re_\theta = 1450$) in the PIV measurement of Kiesow & Plesniak (2003). In § 5, the effects of Reynolds number will be discussed mainly at these two stations.

3. Basic features of a spatially developing non-equilibrium 3DTBL

In this section, we explain the basic features of a spatially developing shear-driven non-equilibrium 3DTBL by showing some mean and turbulence statistics for $Re_{\theta_0} = 300$ with $W_S/U_0 = 1$. In this case, the surface spanwise velocity W_S is equal to the free-stream

velocity U_0. The mean flow direction thus becomes $\tan^{-1}(W_S/U_0) = -45^\circ$ when the collateral state is established.

3.1. *Value of L_{x,W_S} and approach to the collateral state*

We first discuss the value of L_{x,W_S} in the current 3DTBL simulation. Given that Lohmann (1976) reported in his spinning cylinder experiment that the transverse mean velocity and wall shear-stress component attain an asymptotic state in the streamwise distance of approximately $10\delta_0$, we here examine three cases with different values of L_{x,W_S}, i.e. $L_{x,W_S} = 100\theta_0$, $200\theta_0$ and $300\theta_0$ (or, equivalently, $12\delta_0$, $24\delta_0$ and $36\delta_0$), where $L_{Ws1} = 100\theta_0$ and $L_{Ws2} = 200\theta_0$, $300\theta_0$ and $400\theta_0$.

Figure 2(*a*,*b*) shows the distributions of the streamwise and spanwise skin friction coefficients, $C_{f,x} \equiv \tau_{w,x}/(\rho U_0^2/2)$ and $C_{f,z} \equiv \tau_{w,z}/(\rho U_0^2/2)$, as a function of x/θ_0. Note that $\tau_{w,x} \equiv \mu(\partial\bar{U}/\partial y)|_w$ and $\tau_{w,z} \equiv \mu(\partial(\bar{W} - W_S)/\partial y)|_w$, where $\mu = \nu/\rho$. After imposing W_S, $C_{f,x}$ decreases abruptly, due to a non-equilibrium effect (disorganization of the near-wall turbulence). This drop would not appear in a laminar flow since the independence principle, traditionally proposed for swept wings, holds exactly there (this was pointed out by Dr P. R. Spalart, private communication 2019) (see also McLean 2013; Coleman *et al*. 2019). After this drop, $C_{f,x}$ and $C_{f,z}$ increase significantly with increasing x. We then see a near-plateau in the region $x \geq 250\theta_0$ and $x \geq 200\theta_0$ for $C_{f,x}$ and $C_{f,z}$, respectively. The angle of the mean wall shear stress, i.e. $\tan^{-1}(C_{f,z}/C_{f,x})$ (figure 2*c*), however, does not approach -45°, the latter angle being expected when the collateral state is established. Also, the magnitude of $C_{f,x}$ in the collateral boundary layer is estimated to be a factor of $2^{1/2}$ (i.e. $2\cos(-45^\circ)$) larger than that in a 2DTBL since, in the collateral boundary layer, U_0^2 is replaced by $U_0^2 + W_S^2$. Figure 2(*a*) highlights that the approach to a normal 2DTBL is slow for $C_{f,x}$. An estimate of L_{x,W_S} from figure 2 for reaching the collateral state for $Re_{\theta_0} = 300$ would be approximately $1000\theta_0$ (or, equivalently, approximately $100\delta_0$). This condition is a factor of 10 larger than that of Lohmann (1976).

Figure 3 shows the distribution of the mean velocity magnitude normalized by the friction velocity, $Q_r^+ (= Q_r/U_\tau)$, at a downstream station $x/\theta_0 = 350$ for the case with $L_{x,W_S} = 300\theta_0$. Note that the friction velocity in a non-zero cross-flow ($\overline{W} \neq 0$) region (i.e. $L_{Ws1} \leq x \leq L_x$) is obtained such that

$$U_\tau \equiv ([\tau_{w,x}^2 + \tau_{w,z}^2]^{1/2}/\rho)^{1/2}. \tag{3.1}$$

While $C_{f,x}$ exhibits a near-plateau at this station, the agreement between Q_r/U_τ and $\overline{U}/U_{\tau,x}$ is confined to the near-wall region, i.e. there is a departure from the collateral state (i.e. (1.5) and (1.6)) away from the wall. In particular, the magnitude of Q_r/U_τ is smaller than that of $\overline{U}/U_{\tau,x}$ obtained from the 2DTBL simulation. On the other hand, the distribution of $\overline{W}/U_{\tau,z}$ follows the collateral relation (1.4) reasonably well (note that $U_{\tau,z} \equiv \left(\tau_{w,z}/\rho\right)^{1/2}$). This indicates that the mean spanwise velocity develops faster than the mean streamwise velocity. This latter behaviour will also be discussed further in § 5.

3.2. *Relationship between the streamwise velocity deficit and inviscid skewing*

As was mentioned in the introduction, there is close association between the mean streamwise velocity deficit $\partial\overline{U}/\partial x < 0$ and inviscid skewing $\partial\overline{W}/\partial x$ (see (1.5) and (1.6)).

Figure 4 shows the contours in the x–y plane of non-dimensionalized $\overline{\Omega}_x$, $\partial\overline{U}/\partial x$ and $\partial\overline{W}/\partial x$. In the region where W_S is imposed, $\overline{\Omega}_x$ (i.e. mean streamwise vorticity)

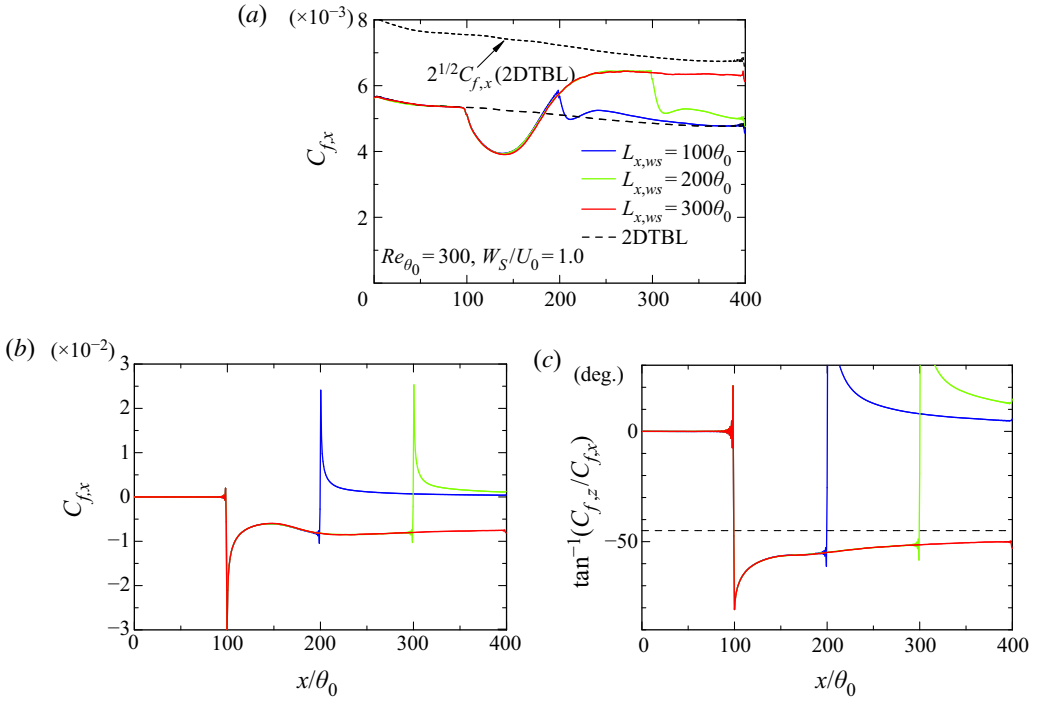

FIGURE 2. Distributions of (*a*) $C_{f,x}$, (*b*) $C_{f,z}$ and (*c*) $\tan^{-1}(C_{f,z}/C_{f,x})$ as functions of x/θ_0 for $Re_{\theta_0} = 300$ with $W_S/U_0 = 1$. The data shown have been obtained with $L_{x,W_S} = 100\theta_0$, $200\theta_0$ and $300\theta_0$.

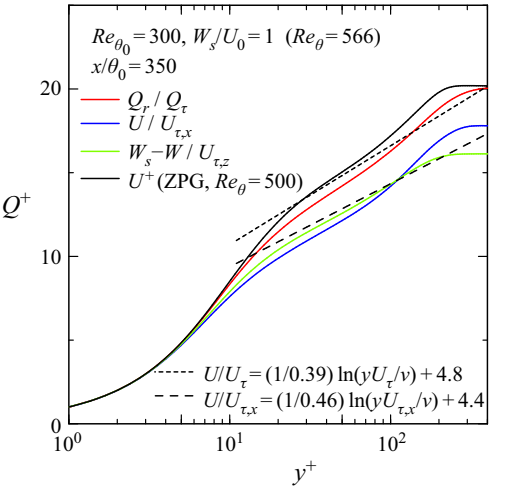

FIGURE 3. Distributions of the normalized mean velocity magnitude Q_r for $Re_{\theta_0} = 300$ with $W_S/U_0 = 1$ at a downstream station of a 3DTBL ($x/\theta_0 = 350$). The data shown have been obtained with $L_{x,W_S} = 300\theta_0$.

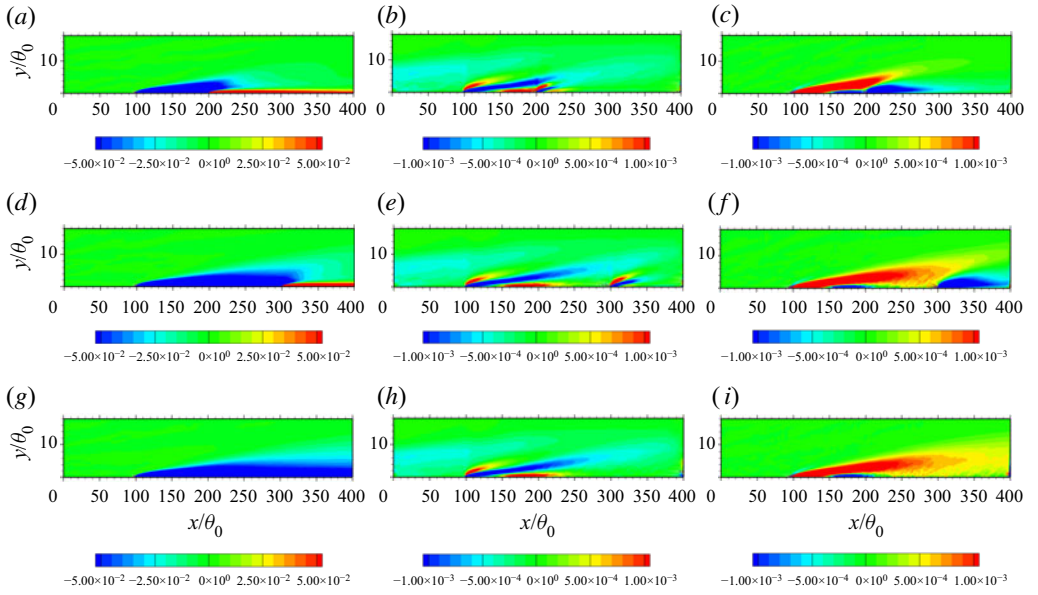

FIGURE 4. Contours in the x–y plane of the normalized $\overline{\Omega}_x$, $\partial\overline{U}/\partial x$ and $\partial\overline{W}/\partial x$ for $Re_{\theta_0} = 300$ with $W_S/U_0 = 1$ using $L_{x,W_S} = 100\theta_0$ (*a–c*), $200\theta_0$ (*d–f*) and $300\theta_0$ (*g–i*): (*a*,*d*,*g*) $(\theta_0/U_0)\overline{\Omega}_x$; (*b*,*e*,*h*) $(\theta_0/U_0)(\partial\overline{U}/\partial x)$; and (*c*,*f*,*i*) $(\theta_0/U_0)(\partial\overline{W}/\partial x)$.

increasingly diffuses towards the outer region until $x/\theta_0 = 250$. In the region $x/\theta_0 \leq 250$, there is indeed a close relationship between inviscid skewing ($\partial\overline{W}/\partial x > 0$) and mean streamwise velocity deficit ($\partial\overline{U}/\partial x < 0$). After $x/\theta_0 = 250$, the development of $\overline{\Omega}_x$ becomes increasingly small as we move downstream for the two cases using $L_{x,W_S} = 200\theta_0$ and $300\theta_0$, where the regions of $\partial\overline{U}/\partial x < 0$ and $\partial\overline{W}/\partial x > 0$ become small, and $C_{f,x}$ exhibits near-constancy. Note that, when $L_{x,W_S} = 100\theta_0$ and $200\theta_0$, there are two transitions from a 2DTBL to a 3DTBL and from a 3DTBL to a 2DTBL. Even in these transitions, we do not observe mean streamwise circulation in the 3DTBL region, but see a streamwise development of the mean streamwise vorticity (see figure 4).

The degree of skewing (turning) of the present 3DTBL can readily be confirmed in mean velocity hodographs (figure 5*a*). At a downstream station of a 3DTBL where $C_{f,x}$ starts to exhibit a plateau (i.e. $x = 250\theta_0$), the profiles (the red lines) follow the linear solid line with the slope of -1.25. The value of arctan (-1.25) is approximately -51°, which agrees well with the direction of the surface shear stress, i.e. $\tan^{-1}(C_{f,z}/C_{f,x})$ (see figure 2*c*). This result indicates that the mean flow has a constant flow angle near the wall. It is well recognized that, for a small turning angle, the spanwise velocity gradient angle is often approximated by the Squire–Winter–Hawthorne equation, i.e.

$$\frac{\partial}{\partial x}\left(\frac{\partial\overline{W}/\partial y}{\partial\overline{U}/\partial y}\right) = \frac{\partial}{\partial x}\left(\frac{\overline{W}}{\overline{U}}\right) \tag{3.2}$$

(see Bradshaw 1987). Note that the minus sign is omitted on the right-hand side of (3.2) since $\partial\overline{W}/\partial y < 0$ in the present flow. Figure 5(*a*,*b*) indicates that relation (3.2) holds reasonably at a downstream station of a 3DTBL (see the red lines representing the profiles at $x = 250\theta_0$). The same is, however, not true for the Reynolds shear stress, i.e. there is a

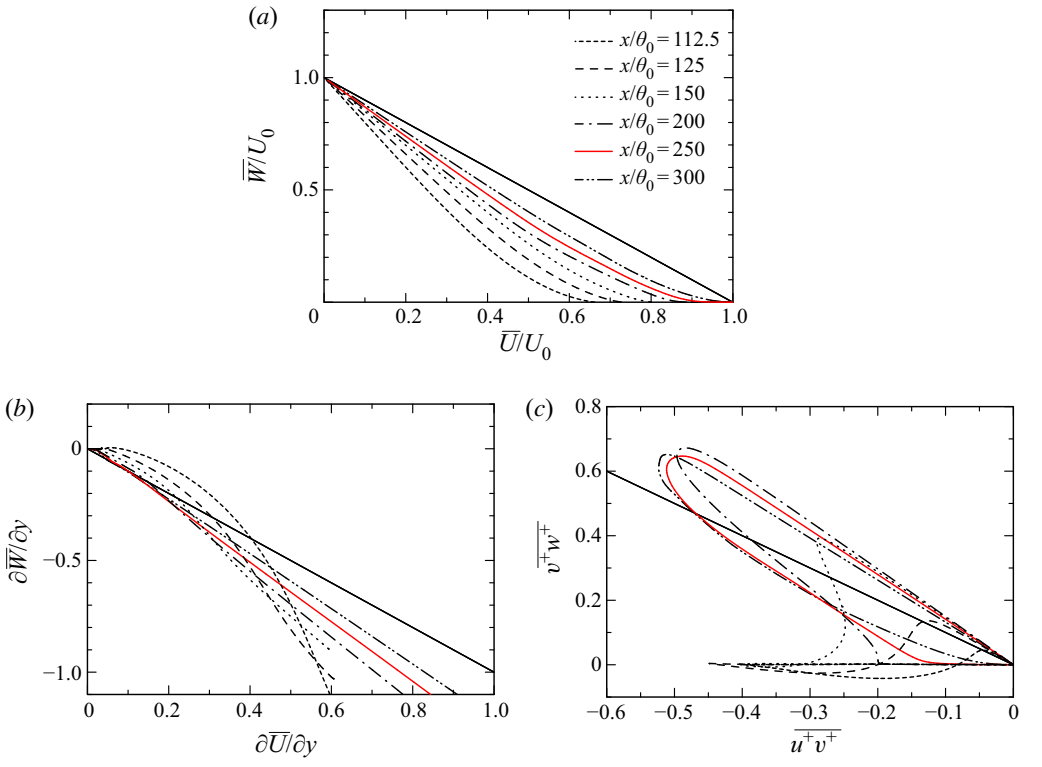

FIGURE 5. Hodograph plots in the 3DTBL region for $Re_{\theta_0} = 300$ with $W_S/U_0 = 1$: (*a*) mean velocity hodograph; (*b*) mean strain-rate hodograph; and (*c*) Reynolds shear-stress hodograph. The red lines refer to the data at $x/\theta_0 = 250$ where a near-plateau has been established in $C_{f,x}$. The data shown have been obtained with $L_{x,W_S} = 300\theta_0$. In (*b*), normalization is made with U_0 and θ_0.

larger departure from the -1.25 slope for the Reynolds stress hodograph (figure 5*c*) than for the mean strain-rate one (figure 5*b*). This underlines that the Reynolds shear stress lags behind the mean strain rate in the 3DTBL region.

3.3. *Basic statistics in the present non-equilibrium 3DTBL*

Here, we explain the basic features of the present non-equilibrium 3DTBL by showing mean velocities and some turbulence statistics for the case using $L_{x,W_S} = 300\theta_0$.

Figure 6 shows the distributions of outer-normalized mean velocities (i.e. $\overline{U}/U_0$ and $\overline{W}/U_0$) and Reynolds shear stresses (i.e. $-\overline{uv}/U_0^2$ and $\overline{vw}/U_0^2$) at several x stations in a 3DTBL region. After imposing W_S, $\overline{W}$ (i.e. cross-flow) increasingly develops from the near-wall region to the outer layer (see figure 6*b*), where the secondary Reynolds shear stress $\overline{vw}$ builds up – this quantity is amplified due to the production term $-\overline{vv}(\partial\overline{W}/\partial y)$ (the distribution is not shown here) – and the latter magnitude increases as x increases (figure 6*d*). On the other hand, the magnitude of $\overline{U}$ is decreased in a 3DTBL region (see figure 6*a*) where there is reduction in the magnitude of $\overline{uv}$; the decreased $\overline{uv}$ propagates outwards with increasing x (see figure 6*c*). Lohmann (1976) noted that the increase in Reynolds stress causes an increasing velocity deficit to develop in the inner part of a 3DTBL. Kiesow & Plesniak (2003) explained that the deficit of $\overline{U}$ results from an increase in the streamwise wall shear stress. The present results indicate that the decreased

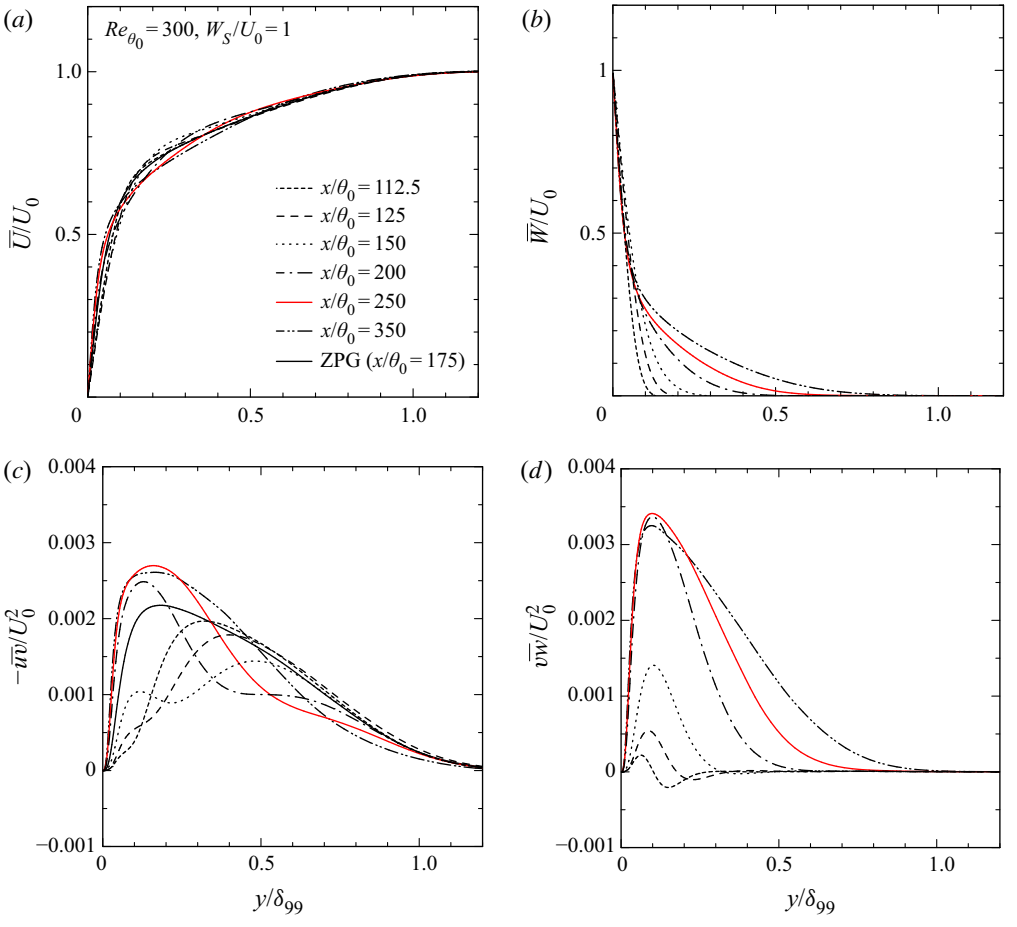

FIGURE 6. Distributions of normalized $\overline{U}$, $\overline{W}$, $\overline{uv}$ and $\overline{vw}$ in the 3DTBL region for $Re_{\theta_0} = 300$ with $W_S/U_0 = 1$: (*a*) $\overline{U}/U_0$; (*b*) $\overline{W}/U_0$; (*c*) $-\overline{uv}/U_0^2$; and (*d*) $\overline{vw}/U_0^2$. The red lines refer to the data at $x/\theta_0 = 250$ where a near-plateau has been established in $C_{f,x}$. The data shown have been obtained with $L_{x,W_S} = 300\theta_0$.

magnitude of $\overline{U}/U_0$ is intrinsically associated with inviscid skewing (see figure 4, where the region of $\partial\overline{W}/\partial x > 0$ corresponds well with that of $\partial\overline{U}/\partial x < 0$), consistent with the finding of Coleman *et al.* (2000) in their temporally developing DNS for an idealization of pressure-driven TBLs.

At a downstream station of a 3DTBL, the magnitude of $-\overline{uv}/U_0^2$ is smaller than that of $\overline{vw}/U_0^2$ (see figure 6*c*,*d*), which is intrinsically associated with the inefficiency in extracting energy from mean flow, as will be discussed in §§ 4.1 and 5.1. The decreased magnitude of $-\overline{uv}/U_0^2$ implies a lag between the Reynolds shear stress and mean strain-rate vectors (see the discussion in § 3.2). Note that the reduced $\overline{uv}$ is not observed in the 3-D channel DNS of Lozano-Durán *et al.* (2020) at a low Reynolds number (i.e. $Re_\tau = 180$), although in both the present and their simulations, $\overline{\Omega}_x$ propagates from the near-wall region to the outer layer. This difference seems to be that between internal and external flows (i.e. channel and boundary layer) since a channel flow has two walls and is likely to suffer from the effect of insufficient scale separation at low Reynolds number.

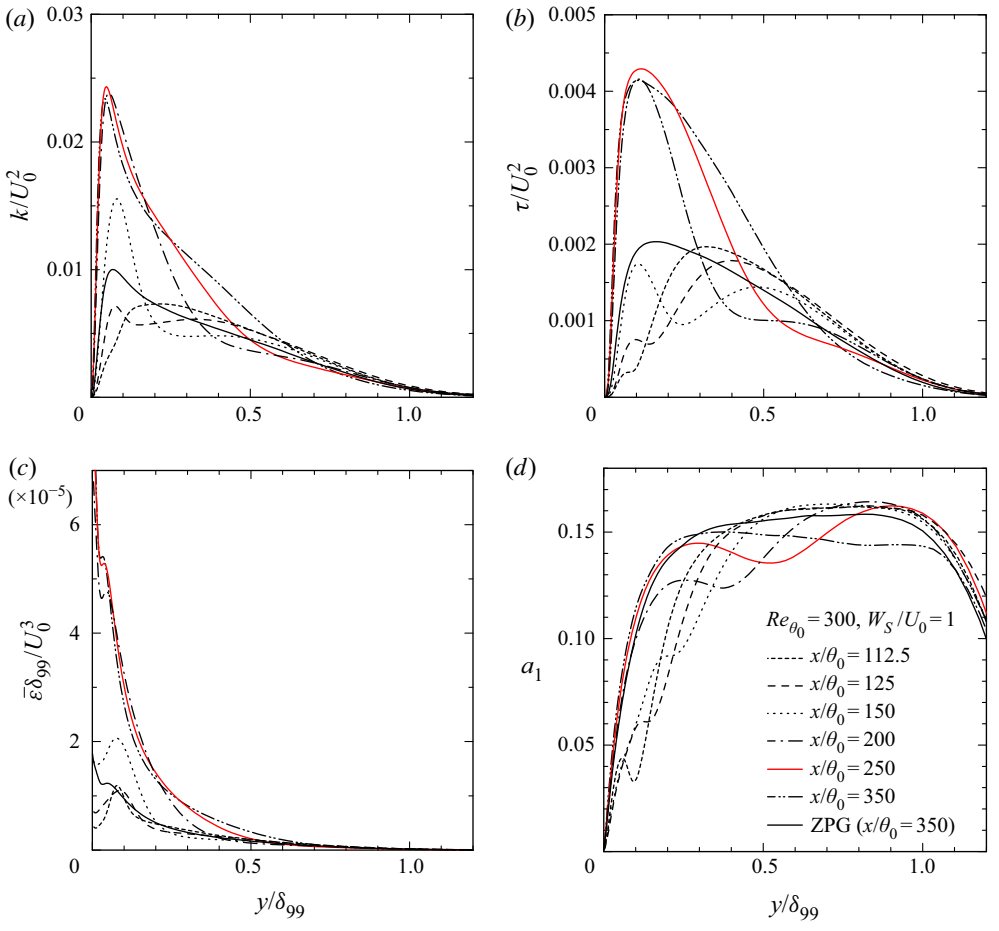

FIGURE 7. Distributions of (*a*) k/U_0^2, (*b*) $\tau/\rho U_0^2$, (*c*) $\overline{\varepsilon}\delta_{99}/U_0^3$ and (*d*) a_1 in the 3DTBL region for $Re_{\theta_0} = 300$ with $W_S/U_0 = 1$. The red lines refer to the data at $x/\theta_0 = 250$ where a near-plateau has been established in $C_{f,x}$. The data shown have been obtained with $L_{x,W_S} = 300\theta_0$.

On the other hand, the present 3DTBL increasingly develops from the near-wall region towards the outer region (this latter region is initially a 2DTBL) by inviscid skewing (i.e. three-dimensionality). The reduced $\overline{uv}$ is thus observed independent of Reynolds number. The reason for the decrease in $\overline{uv}$ will be discussed in § 5.4.

As for the turbulence statistics, there is a sudden decrease in the magnitudes of the turbulent kinetic energy k (figure 7*a*), the total Reynolds shear stress $\tau \equiv (\overline{vw}^2 + \overline{uv}^2)^{1/2}$ (figure 7*b*) and the energy dissipation rate $\overline{\varepsilon} \equiv \nu\overline{u_{i,j}(u_{i,j} + u_{j,i})}$ (figure 7*c*) in the region $x/\theta_0 = 100 \sim 125$. A similar decrease is found for the temporally developing DNS of Moin *et al.* (1990) and Coleman *et al.* (1996), which is attributed to a non-equilibrium effect. After this drop, the near-wall magnitudes of k/U_0^2, τ/U_0^2 and $\overline{\varepsilon}\delta_{99}/U_0^3$ increase with x. In particular, $\overline{\varepsilon}\delta_{99}/U_0^3$ exhibits a larger magnitude close to a wall than that for a 2DTBL (figure 7*c*), qualitatively similar to those observed in the temporally developing DNS of Moin *et al.* (1990). At $x/\theta_0 = 250$ (see the red lines in figure 7), the increase in k/U_0^2 and τ/U_0^2 from a 2DTBL is approximately a factor of 2. The latter factor is estimated by

considering the collateral boundary layer where U_0^2 is replaced by $U_0^2 + W_S^2$. This indicates that the turbulence develops by cross-flow (arising from W_S) effectively in a 3DTBL, although the Reynolds stress anisotropy is not altered adequately with this short transition length (see figure 6, where the peak magnitude of $-\overline{uv}/U_0^2$ is smaller than that of $\overline{vw}/U_0^2$).

Also, it would be instructive to address how the structure parameter a_1 varies on moving downstream in the present 3DTBL given that significant attention has been paid to this quantity in the earlier experimental and DNS works. Figure 7(*d*) shows the distributions of the structure parameter a_1 in terms of y/δ_{99} in the 3DTBL region (note that δ_{99} denotes the 99 % boundary layer thickness). After the initial drop, the magnitude of a_1 tends to approach that of a 2DTBL at $x/\theta_0 = 250$ below $y/\delta_{99} = 0.2$, consistent with the behaviour of k/U_0^2 and τ/U_0^2. The approach to the 2DTBL is also observed in the equilibrium 3DTBL simulations (Spalart 1989; Wu & Squires 1997). There is, however, a decrease in the magnitude of a_1 away from the wall (figure 7*d*) owing to the reduction of τ (figure 7*b*). Note that the y location at which a_1 exhibits a decreased magnitude moves outwards with increasing x, whereas for $\overline{uv}$, the decrease is not observed for a_1 at a low Reynolds number in a 3-D channel DNS of Lozano-Durán *et al*. (2020).

4. Effect of cross-flow

Here, we investigate the effect of cross-flow in a shear-driven non-equilibrium 3DTBL for $Re_{\theta_0} = 300$ with varying W_S, *viz.* $W_S/U_0 = 0$, 0.1, 0.5, 1.0, 1.5 and 2.0. For this purpose, we here use $L_{x,W_S} = 200\theta_0$ (or, equivalently, $24\delta_0$), where $L_{Ws1} = 100\theta_0$ and $L_{Ws2} = 300\theta_0$. In this case, a near-plateau is obtained for both the streamwise and spanwise skin friction coefficients in the 3DTBL region ($x \geq 250\theta_0$) at this inlet Reynolds number (i.e. $Re_{\theta_0} = 300$).

4.1. *Skin friction coefficients*

Figure 8(*a*,*b*) shows the distributions of the streamwise and spanwise skin friction coefficients, $C_{f,x}$ and $C_{f,z}$, as a function of x/θ_0. After imposing W_S, $C_{f,x}$ decreases abruptly in the 3DTBL region (i.e. $100 \leq x/\theta_0 \leq 300$) when $W_S/U_0 \geq 0.5$. This is due to a non-equilibrium effect. After this decrease, $C_{f,x}$ and $C_{f,z}$ increase significantly with increasing W_S. The rates of increase in $C_{f,x}$ and $C_{f,z}$ from $W_S/U_0 = 1$ and 2 (i.e. $\tan^{-1}(W_S/U_0) = -45^\circ$ and -63°) are approximately 1.2 and 2.5, respectively, at $x/\theta_0 \approx 250$, while 1.5 ($= 5\cos(-63^\circ)/2\cos(-45^\circ)$) and 3.0 ($= 5\sin(-63^\circ)/2\sin(-45^\circ)$) are estimated from the collateral state. The approach to the collateral state is slower for $C_{f,x}$ than for $C_{f,z}$, which is intrinsically associated with the inefficiency in extracting energy from mean flow by the Reynolds shear stress $-\overline{uv}$. This point will be discussed below.

For $C_{f,z}$, Kannepalli & Piomelli (2000) proposed a mixed scaling such that

$$C_{f,z\,mixed} = \tau_{w,z}/(\rho U_0 W_S/2). \tag{4.1}$$

Figure 8(*c*) demonstrates that this scaling holds reasonably well for $W_S/U_0 \leq 1$, but not for $W_S/U_0 > 1$ inside the 3DTBL region ($100 \leq x/\theta_0 \leq 300$). This is essentially associated with the departure from the half-power law of θ_z, as will be discussed in § 5 (see figure 13*b*). On the other hand, (4.1) holds excellently in the recovery region ($300 \leq x/\theta_0 \leq 400$) independent of W_S. The forcing (i.e. the imposition of W_S) thus most likely yields the departure from (4.1).

To gain further insight into the behaviour of the skin friction coefficients, we here examine the mean energy balance, by referring to the work of Renard & Deck (2016)

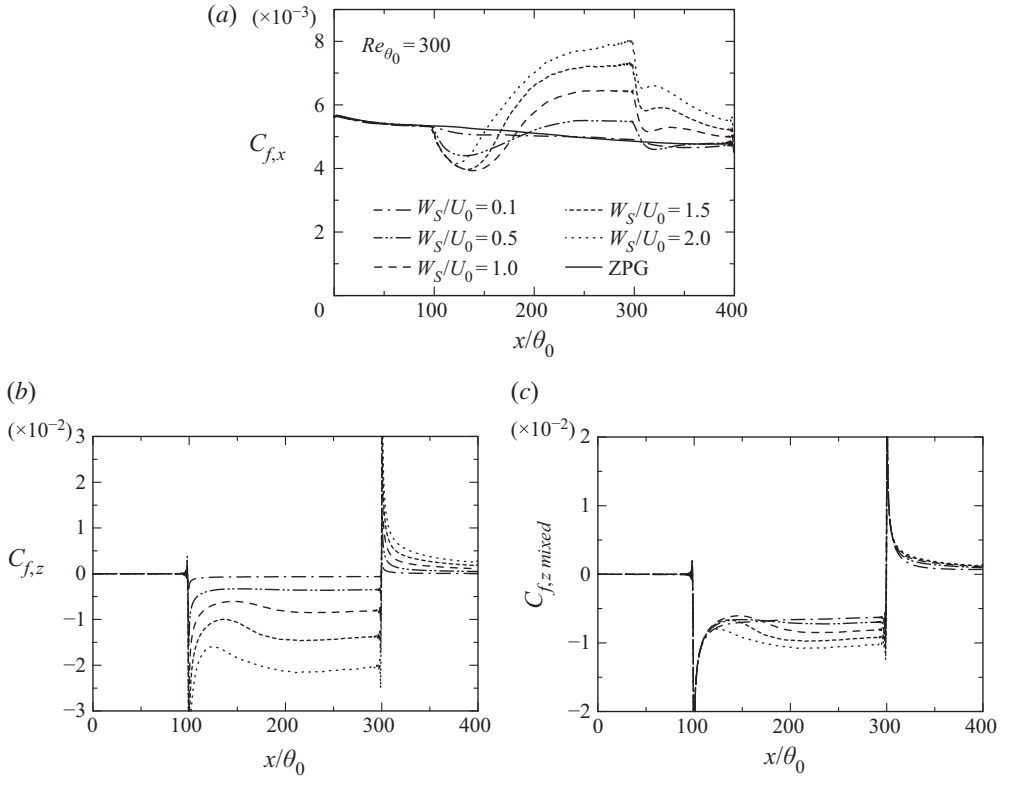

FIGURE 8. Distributions of (*a*) $C_{f,x}$, (*b*) $C_{f,z}$ and (*c*) $C_{f,z\,mixed}$ as functions of x/θ_0 for $Re_{\theta_0} = 300$ with varying W_S. The data shown have been obtained with $L_{x,W_S} = 200\theta_0$.

in a 2DTBL, for the streamwise skin friction coefficient $C_{f,x}$, i.e.

$$C_{f,x} = \underbrace{\frac{2}{U_0^3}\int_0^\infty \nu\left(\frac{\partial \overline{U}}{\partial y}\right)^2 \mathrm{d}y}_{C_{f,x\,vis}} + \underbrace{\frac{2}{U_0^3}\int_0^\infty \left(-\overline{uu}\frac{\partial \overline{U}}{\partial x} - \overline{uv}\frac{\partial \overline{U}}{\partial y}\right)\mathrm{d}y}_{C_{f,x\,turb}} + \underbrace{\frac{2}{U_0^3}\int_0^\infty (\overline{U} - U_0)\left(\overline{U}\frac{\partial \overline{U}}{\partial x} + \overline{V}\frac{\partial \overline{U}}{\partial y}\right)\mathrm{d}y}_{C_{f,x\,conv}}. \tag{4.2}$$

Note that the x derivative term is included in the second term on the right-hand side in (4.2) since this term may not be dismissed in a 3DTBL. Using a boundary layer approximation and by multiplying the relation for the total streamwise shear stress, *viz.*

$$\frac{\tau_{x\,total}}{\rho} = \nu\left(\frac{\partial \overline{U}}{\partial y}\right) - \overline{uv}, \tag{4.3}$$

by $\partial \overline{U}/\partial y$, Rotta (1962) obtained the following relation:

$$\frac{1}{\rho}\frac{\partial \tau_{w,x}\bar{U}}{\partial y} = -\overline{uv}\frac{\partial \bar{U}}{\partial y} + \nu\left(\frac{\partial \bar{U}}{\partial y}\right)^2. \tag{4.4}$$

Here, $(1/\rho)(\partial\tau_{w,x}\overline{U}/\partial y)$ represents the rate of energy transfer from the outer part of the boundary layer to the inner region. The energy is partly dissipated directly by viscosity (the second term on the right-hand side of (4.4)) and partly extracted to turbulence via the work done by the primary Reynolds shear stress $-\overline{uv}$ (the first term on the right-hand side of (4.4)). The integrals of (4.2) thus represent the amounts of direct viscous dissipation (the first term on the right), the energy extracted from the mean flow by the work of the Reynolds stress (the second term on the right) and that associated with convection (the third term on the right).

Similarly, the transverse skin friction coefficient $C_{f,z}$ may be expressed as

$$C_{f,z} = \underbrace{-\frac{2}{U_0^2 W_S}\int_0^\infty \nu\left(\frac{\partial\overline{W}-W_S}{\partial y}\right)^2 \mathrm{d}y}_{C_{f,z\,vis}} \underbrace{-\frac{2}{U_0^2 W_S}\int_0^\infty \left(-\overline{uw}\frac{\partial\overline{W}}{\partial x}-\overline{vw}\frac{\partial\overline{W}}{\partial y}\right)\mathrm{d}y}_{C_{f,z\,turb}} \underbrace{-\frac{2}{U_0^2 W_S}\int_0^\infty \overline{W}\left(\overline{U}\frac{\partial\overline{W}}{\partial x}+\overline{V}\frac{\partial\overline{W}}{\partial y}\right)\mathrm{d}y}_{C_{f,z\,conv}}. \tag{4.5}$$

Note that the total spanwise shear stress may be written as

$$\frac{\tau_{z\,total}}{\rho} = \nu\left(\frac{\partial\overline{W}-W_S}{\partial y}\right) - \overline{vw}. \tag{4.6}$$

In (4.5) and (4.6), $W_S = 0$ outside the 3DTBL region (i.e. $100 \le x/\theta_0 \le 300$).

Figure 9(*a*) shows the distributions of normalized $C_{f,x\,vis}$, $C_{f,x\,turb}$ and $C_{f,x\,conv}$ in (4.2) as a function of x/θ_0 for $Re_{\theta_0} = 300$ with $W_S/U_0 = 1.0$. While the magnitude of $C_{f,x\,turb}$ is smaller than that of $C_{f,x\,vis}$ in a 2DTBL, the relative magnitude of $C_{f,x\,turb}$ to $C_{f,x\,vis}$ is increased in a 3DTBL due to the increased mean straining, so that they are nearly equal at a downstream station of a 3DTBL. The magnitudes of $C_{f,z\,turb}$ and $C_{f,z\,viz}$ are also almost the same in a 3DTBL for $Re_{\theta_0} = 300$ with $W_S/U_0 = 1.0$ (the distributions are not shown here). The magnitudes of the viscous and turbulent parts in (4.2) and (4.5), however, depend intrinsically on W_S in a 3DTBL. Here, we normalize the skin friction coefficients by $(C_f^{3/2}/2^{1/2})$, which yields the inner-normalized integral (i.e. U_0/U_τ) and may readily be compared with the analysis in 2-D flows by Renard & Deck (2016), Abe & Antonia (2016) and Wei (2018). Figure 9(*b*) shows the distributions of $(2^{1/2}/C_f^{3/2})C_{f,x\,vis}$ for $Re_{\theta_0} = 300$ with varying W_S. In the 2DTBL region ($0 \le x/\theta_0 \le 100$), the current result is essentially identical with that ($= 9.13$) in a 2-D flow by Renard & Deck (2016), Abe & Antonia (2016) and Wei (2018). In the 3DTBL region ($100 \le x/\theta_0 \le 300$), the magnitude of $(2^{1/2}/C_f^{3/2})C_{f,x\,vis}$ decreases significantly with increasing W_S due to the change of the surface shear-stress direction.

As for the turbulent parts in (4.2) and (4.5), the magnitudes of $(2^{1/2}/C_f^{3/2})C_{f,x\,turb}$ and $(2^{1/2}/C_f^{3/2})C_{f,z\,turb}$ are decreased and increased, respectively, in a 3DTBL with increasing W_S for $W_S/U_0 \le 1.0$ (see figure 9*c*,*d*). When $W_S/U_0 = 1$, the magnitude of $(2^{1/2}/C_f^{3/2})C_{f,z\,turb}$ is 30 % greater than $(2^{1/2}/C_f^{3/2})C_{f,x\,turb}$ (note that $C_{f,x\,turb} = C_{f,z\,turb}$ is expected in the collateral state). This result highlights that, in a non-equilibrium 3DTBL, the primary Reynolds shear stress $\overline{uv}$ is less efficient in extracting energy from the

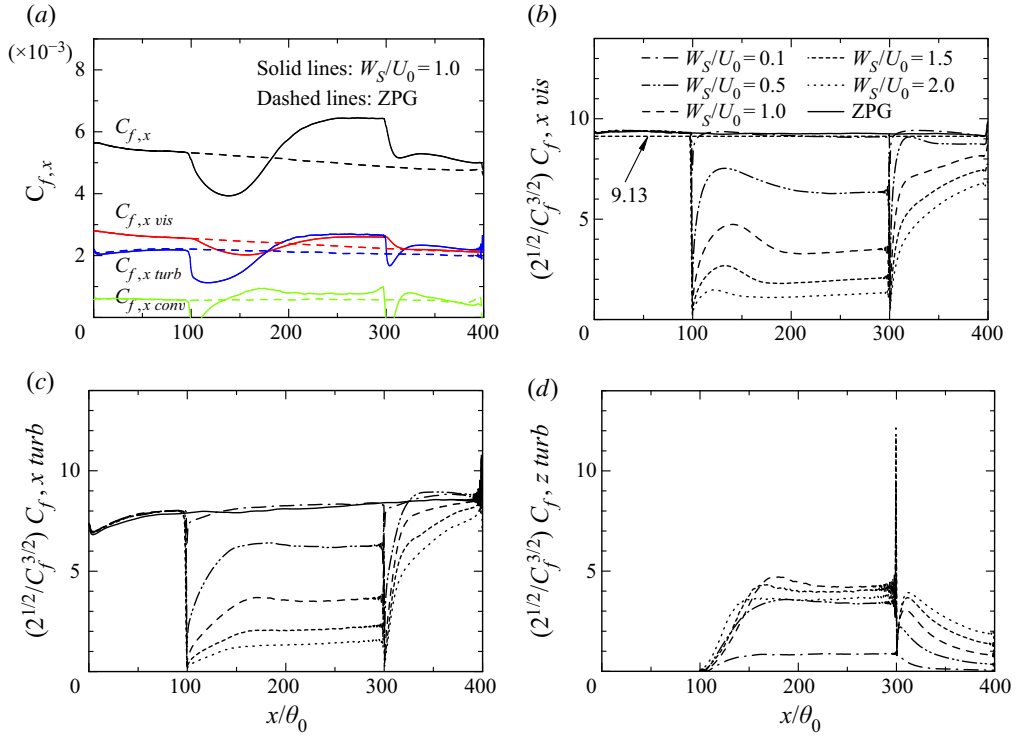

FIGURE 9. Distributions of terms on the right-hand side of (4.2) and (4.5) as functions of x/θ_0 for $Re_{\theta_0} = 300$: (*a*) $C_{f,x\ vis}$, $C_{f,x\ turb}$ and $C_{f,x\ conv}$ with $W_S/U_0 = 1$; (*b*) $(2^{1/2}/{C_f}^{3/2})C_{f,x\ vis}$ with varying W_S; (*c*) $(2^{1/2}/{C_f}^{3/2})C_{f,x\ turb}$ with varying W_S; and (*d*) $(2^{1/2}/{C_f}^{3/2})C_{f,z\ turb}$ with varying W_S. The data shown have been obtained with $L_{x,W_S} = 200\theta_0$.

mean flow than the secondary Reynolds shear stress $\overline{vw}$. For $W_S/U_0 \geq 1.0$, the increase in $(2^{1/2}/C_f^{3/2})C_{f,z\,turb}$ seems to be saturated. This is probably associated with a reduced magnitude of the pressure strain term for $\overline{vv}$ (active motion) as W_S increases given that the production for $\overline{vw}$ consists of the product of $\overline{vv}$ and $(\partial\overline{W}/\partial y)$. The Re dependence will be discussed in § 5.

4.2. *Near-wall streaks and vortical structures*

The increased drag in the 3DTBL region has a close relationship with the energized near-wall vortical structures by cross-flow. Figure 10 shows the isosurfaces of the instantaneous streamwise velocity fluctuation u and a positive value of the second invariant of the velocity gradient tensor $Q(\equiv -u_{i,j}u_{j,i}/2)$ with a magnified view in the near-wall region. After imposing W_S at $x/\theta_0 = 100$, the near-wall streaks and quasi-streamwise vortices are weakened due to a non-equilibrium effect. The latter becomes more pronounced as W_S increases. On moving downstream, they then reappear and rotate their directions to those of the surface shear stress. Both the streaks and vortical structures become more energetic with increasing W_S due to the increased straining by cross-flow, indicating that turbulence develops efficiently by cross-flow. In particular, near-wall vortices show a clustering for larger W_S. These behaviours can be quantified by examining the streamwise normal Reynolds stress $\overline{uu}/U_0^2$ and the enstrophy $\overline{\omega_i^*\omega_i^*}$ in the 3DTBL

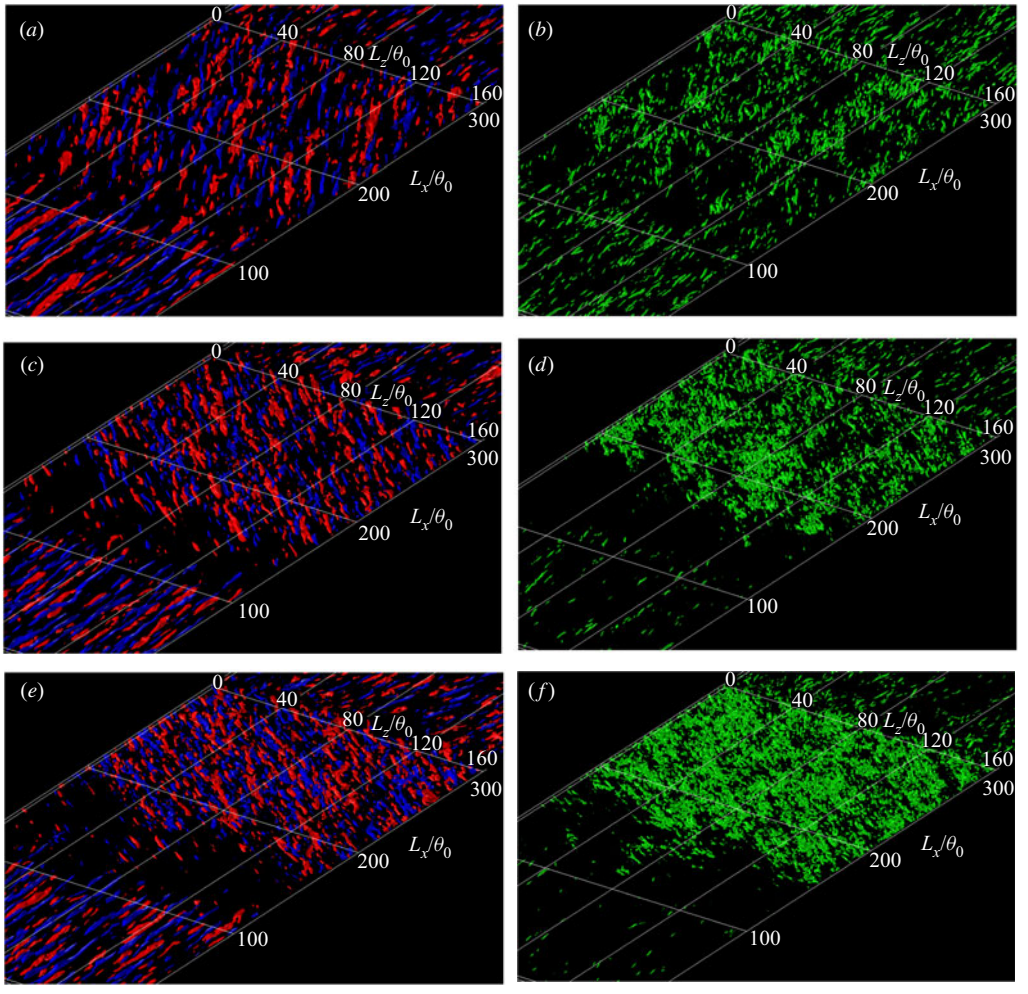

FIGURE 10. Isosurfaces of u and Q for $Re_{\theta_0} = 300$ with $W_S/U_0 = 0.5$, 1.0 and 1.5 : (a,c,e) red, $u/U_0 > 0.15$; blue, $u/U_0 < -0.15$; (b) white, $Q\theta_0^2/U_0^2 > 0.01$; (d) white, $Q\theta_0^2/U_0^2 > 0.02$; (f) white, $Q\theta_0^2/U_0^2 > 0.04$. The fluid flows from bottom left to top right. The magnitudes of W_S/U_0 are 0.5 (a,b), 1.0 (c,d) and 1.5 (e,f), respectively. Note that the data below $y/\delta_{99,0} \approx 0.2$ have been plotted for highlighting the near-wall structures. The data shown have been obtained with $L_{x,W_S} = 200\theta_0$.

region (see figure 11) (note that a superscript * denotes the normalization by U_0 and δ_{99}). Indeed, near-wall $\overline{\omega_i^*\omega_i^*}$ is more increased than $\overline{uu}/U_0^2$ as W_S increases, consistent with the experimental results of Kiesow & Plesniak (2003). The increase is also observed for the energy dissipation rate $\overline{\varepsilon}^*$ (distributions not shown here). This indicates that small scales are affected efficiently by cross-flow due to the increased mean straining. The behaviour of $\overline{\omega_i^*\omega_i^*}$ is also linked to the increased magnitude of the pressure fluctuation (distribution of $p_{rms}/\rho U_0^2$ not shown here), although their characteristic y scales are different (see Abe *et al.* 2018).

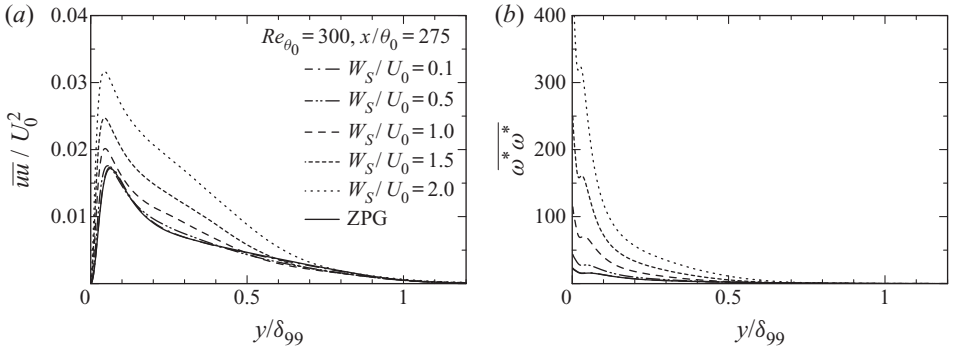

FIGURE 11. Distributions of $\overline{uu}/U_0^2$ and $\overline{\omega_i^*\omega_i^*}$ in the 3DTBL region ($x/\theta_0 = 275$) for $Re_{\theta_0} = 300$ with varying W_S: (*a*) $\overline{uu}/U_0^2$; and (*b*) $\overline{\omega_i^*\omega_i^*}$. The data shown have been obtained with $L_{x,W_S} = 200\theta_0$.

4.3. *Reynolds stress and energy redistribution*

We now discuss the near-wall distributions of the Reynolds stress and the energy redistribution. Figure 12(*a–d*) shows the distributions of the inner-normalized Reynolds normal stresses (i.e. $\overline{u^+u^+}$, $\overline{v^+v^+}$ and $\overline{w^+w^+}$) and Reynolds shear stress (i.e. $-\overline{u^+v^+}$) at a downstream station of the 3DTBL region ($x/\theta_0 = 275$). Whilst all the Reynolds normal stresses normalized by U_0^2 increase with cross-flow, the inner-normalized Reynolds normal stresses exhibit a different behaviour. That is, $\overline{u^+u^+}$ decreases and $\overline{w^+w^+}$ increases (figure 12*a*,*c*) with increasing W_S; and $\overline{v^+v^+}$ (figure 12*b*) decreases slightly. Also, k^+ (not shown here) increases gradually with increasing W_S due to the increase in Reynolds number in a 3DTBL. This indicates that the anisotropy in the Reynolds normal stress is altered with increasing W_S. The primary Reynolds shear stress ($-\overline{u^+v^+}$) also decreases with increasing W_S, as observed in the recent DNS work by Lozano-Durán *et al*. (2020) in a turbulent channel flow with a sudden spanwise pressure gradient. Not only the inactive motion ($\overline{u^+u^+}$ and $\overline{w^+w^+}$) but also the active motion ($\overline{v^+v^+}$ and $-\overline{u^+v^+}$) are changed in a 3DTBL. Note that, given the original idea of Townsend's (1976) hypothesis, 'inactive' denotes a smaller contribution of larger motions to the Reynolds shear stress compared to that of smaller motions, while 'active' refers to the contribution exclusively to the Reynolds shear stress; see § 5.3 of Hwang (2015). In this sense, large scales contain half of the Reynold shear stress in the log region or the outer region of a pipe flow (Guala, Hommema & Adrian 2006) and of a channel and 2DTBL (Balakumar & Adrian 2007) (see also the spectral analysis in § 5.3).

To gain further insight into the variation of the Reynolds stresses, we here examine the pressure strain term (see figure 12*e–h*), which can be obtained by splitting the VPG (Π_{ij}^+) into the pressure strain (ϕ_{ij}^+) and pressure diffusion (φ_{ij}^+) terms, respectively:

$$\Pi_{ij}^+ = \underbrace{\overline{p^+\left(\frac{\partial u_i^+}{\partial x_j^+} + \frac{\partial u_j^+}{\partial x_i^+}\right)}}_{\phi_{ij}^+} - \underbrace{\left(\frac{\partial}{\partial x_i^+}\overline{u_j^+p^+} + \frac{\partial}{\partial x_j^+}\overline{u_i^+p^+}\right)}_{\varphi_{ij}^+}. \tag{4.7}$$

The pressure strain term is responsible for the energy redistribution for the Reynolds normal stress but for the destruction for the Reynolds shear stress. In a 2DTBL, the

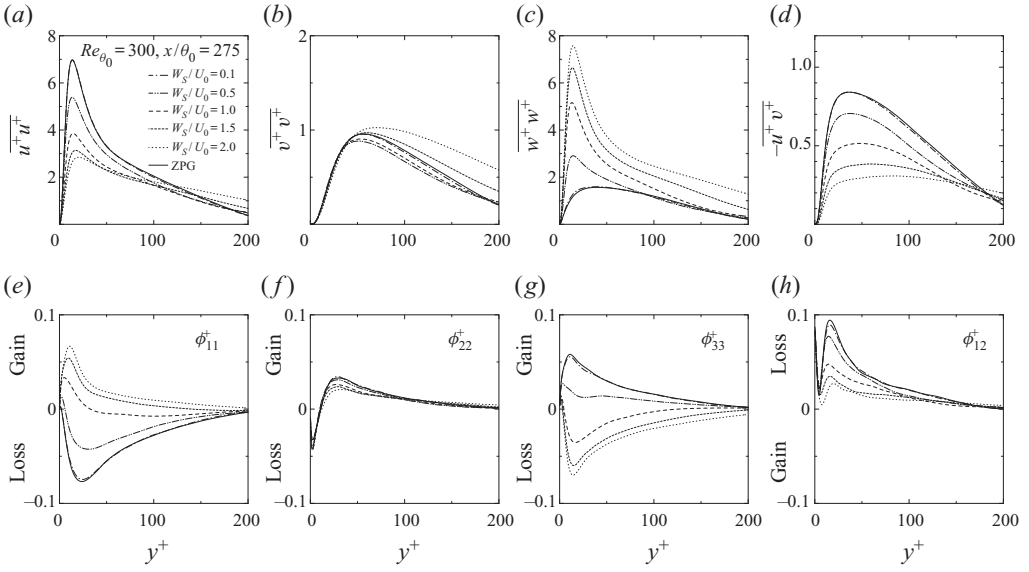

FIGURE 12. Distributions of the inner-normalized Reynolds stresses and the pressure strain terms in the 3DTBL region ($x/\theta_0 = 275$) for $Re_{\theta_0} = 300$ with varying W_S: (*a*) $\overline{u^+u^+}$; (*b*) $\overline{v^+v^+}$; (*c*) $\overline{w^+w^+}$; (*d*) $-\overline{u^+v^+}$; (*e*) ϕ^+_{11}; (*f*) ϕ^+_{22}; (*g*) ϕ^+_{33}; and (*h*) ϕ^+_{12}. The data shown have been obtained with $L_{x,W_S} = 200\theta_0$.

pressure strain plays a role in redistributing the energy from $\overline{uu}$ to $\overline{vv}$ and $\overline{ww}$. In the present 3DTBL, once the magnitude of $\overline{ww}/U_\tau^2$ exceeds that of $\overline{uu}/U_\tau^2$, the pressure strain for $\overline{uu}$ and $\overline{ww}$ show negative and positive values, respectively The energy redistribution for the inactive motion ($\overline{uu}$ and $\overline{ww}$) is indeed varied as the magnitude of cross-flow increases, whereas ϕ^+_{22} for the active motion ($\overline{vv}$) decreases slightly. This indicates that the energy redistributes from $\overline{ww}$ to $\overline{uu}$ in the 3DTBL region when W_S becomes sufficiently large. The largest values of ϕ^+_{11} and ϕ^+_{33} (≈ 0.08) are approximately one-fifth of the maximum value of P^+_{11} (≈ 0.5) in a 2DTBL. The magnitude of ϕ^+_{12} (and thus the active motion) also decreases with increasing W_S, which was recently pointed out by Lozano-Durán *et al.* (2020) in a turbulent channel flow with a sudden spanwise pressure gradient. They associated this behaviour with the self-similar behaviour in a 3DTBL. The self-similarity will be discussed in the next section. The present results indicate that the pressure strain term may not be dismissed when considering the modelling of $\overline{u_i u_j}$ in a 3DTBL.

5. Effect of Reynolds number

In this section, we discuss the *Re* dependence in a shear-driven 3DTBL for three Reynolds numbers ($Re_{\theta_0} = 300$, 600 and 900) with intermediate and large magnitudes of W_S (i.e. $W_S/U_0 = 1$ and 2) by focusing on the behaviours of the mean velocity and the Reynolds stress. For this purpose, we here use $L_{x,W_S} = 100\theta_0$ (or, equivalently, $12\delta_0$) where $L_{W_S1} = 100\theta_0$ and $L_{W_S2} = 200\theta_0$; a near-plateau is obtained in the 3DTBL region for both the streamwise and spanwise skin friction coefficients for $Re_{\theta_0} = 600$ and 900, but not for $Re_{\theta_0} = 300$ (see § 3.1).

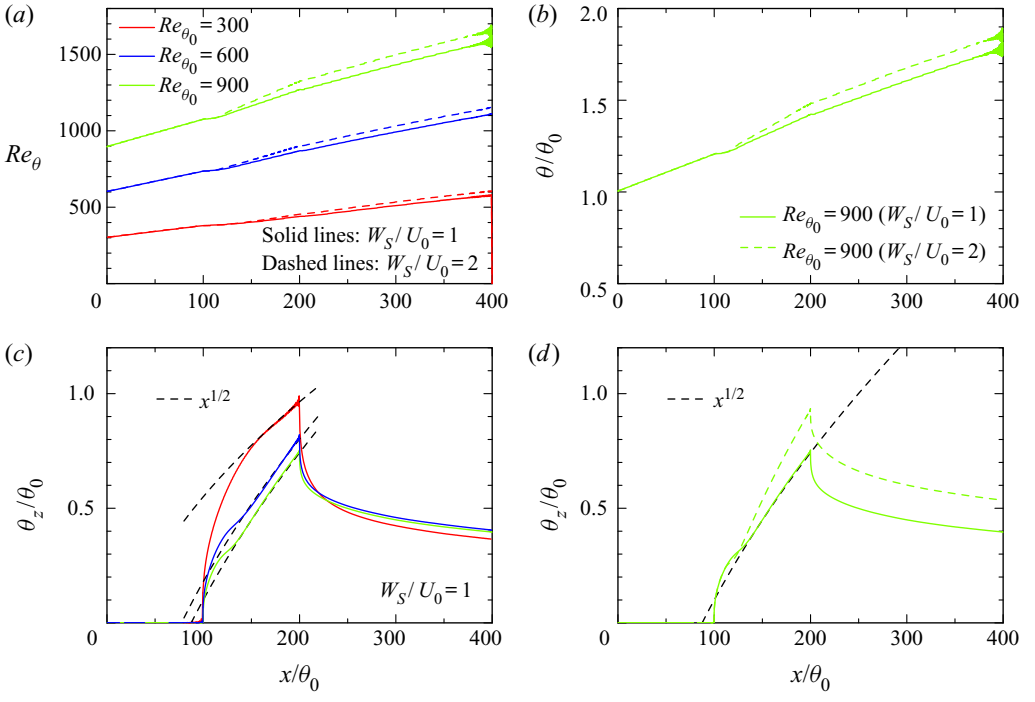

FIGURE 13. Distributions of Re_θ, θ/θ_0 and θ_z/θ_0 as functions of x/θ_0: (*a*) Re_θ; (*b*) θ/θ_0 for $Re_{\theta_0}=900$ with $W_S/U_0=1$ and 2; (*c*) θ_z/θ_0 for $Re_{\theta_0}=300$, 600 and 900 with $W_S/U_0=1$; and (*d*) θ_z/θ_0 for $Re_{\theta_0}=900$ with $W_S/U_0=1$ and 2. The data shown have been obtained with $L_{x,W_S}=100\theta_0$.

5.1. *Momentum thickness and skin friction coefficients*

Figure 13 shows the distributions of the streamwise and spanwise momentum thicknesses, θ and θ_z (*viz.* (1.7) and (1.8)), and the momentum thickness Reynolds number, Re_θ, as a function of x/θ_0. For the streamwise momentum thickness θ, the magnitude increases almost linearly with x/θ_0. The imposition of W_S yields an increase in θ, where the rate of increase is greater for a larger W_S (see figure 13*b*). The increased momentum thickness is essentially associated with inviscid skewing since the latter yields the deficit of $\overline{U}$. The increased magnitude of θ is also linked to that of $C_{f,x}$ (see figure 14*a*) as $\partial\theta/\partial x = C_{f,x}/2$ in the present flow due to the absence of the streamwise mean pressure gradient. The momentum thickness Reynolds number Re_θ thus depends intrinsically on both cross-flow and Reynolds number (see figure 13*a*). For the largest Re_{θ_0} and W_S (i.e. $Re_{\theta_0}=900$ and $W_S/U_0=2$), Re_θ indeed varies from 900 (at the inlet) to 1550 (at the outlet). For the spanwise momentum thickness θ_z, on the other hand, the magnitude for $W_S/U_0=1$ increases with a $x^{1/2}$ dependence in the 3DTBL region for all three Reynolds numbers (see figure 13*c*), which corroborates the LES result of Kannepalli & Piomelli (2000) for $Re_\theta\approx 1100$. The rate of increase for $W_S/U_0=1$ is identical with that of Antonia & Luxton (1971) in their experiment in TBLs on the sudden change of the surface condition. However, θ_z develops more significantly for $W_S/U_0=2$ than for $W_S/U_0=1$, the former showing a departure from a $x^{1/2}$ dependence (see figure 13*d*). This latter trend seems to hold for a further larger W_S. The $x^{1/2}$ behaviour is essentially associated with the Stokes layer $\theta_z=\sqrt{\nu t}$, whereas the departure from the $x^{1/2}$ behaviour is due to the increased

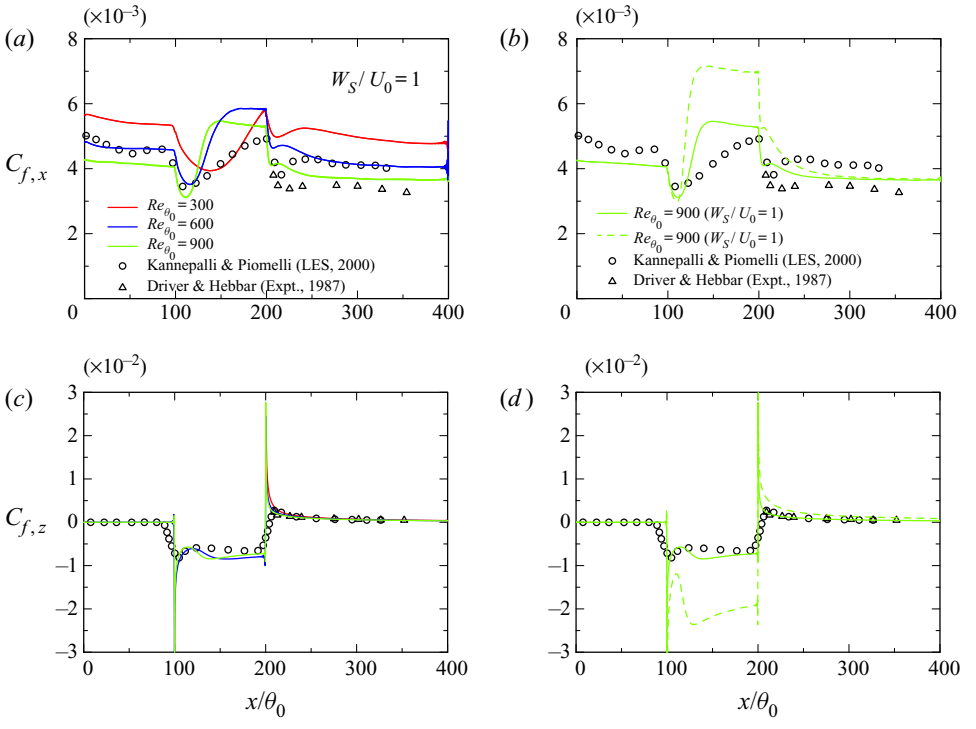

FIGURE 14. Distributions of $C_{f,x}$ and $C_{f,z}$ as functions of x/θ_0: (*a*) $C_{f,x}$ for $Re_{\theta_0} = 300$, 600 and 900 with $W_S/U_0 = 1$; (*b*) $C_{f,x}$ for $Re_{\theta_0} = 900$ with $W_S/U_0 = 1$ and 2; (*c*) $C_{f,z}$ for $Re_{\theta_0} = 300$, 600 and 900 with $W_S/U_0 = 1$; and (*d*) $C_{f,z}$ for $Re_{\theta_0} = 900$ with $W_S/U_0 = 1$ and 2. The data shown have been obtained with $L_{x,W_S} = 100\theta_0$.

turbulent eddy viscosity $\theta_z = \sqrt{\nu_{t,z}t}$ (see figure 22(*b*) where the magnitude of $\nu_{t,z}/\nu_{t,x}$ increases with cross-flow at a large Re). The latter behaviour was also reported in the recent temporally developing DNS work of Lozano-Durán *et al.* (2020).

Figure 14(*a,c*) shows the distributions of the streamwise and spanwise skin friction coefficients, $C_{f,x}$ and $C_{f,z}$, as a function of x/θ_0 for all three Reynolds numbers with $W_S/U_0 = 1$. Also compared are the LES data of Kannepalli & Piomelli (2000) and the experimental data of Driver & Hebbar (1987) – their Reynolds numbers in a near-trailing edge of the 3DTBL region are $Re_\theta \approx 1100$ and 6000, respectively. After imposing W_S, we see a sudden decrease in the magnitudes of $C_{f,x}$ and $C_{f,z}$ for all three Reynolds numbers. The streamwise locations at which both $C_{f,x}$ and $C_{f,z}$ attain near-plateaus become smaller in terms of x/θ_0 as the Reynolds number increases, while that for $C_{f,x}$ is not obtained for $Re_{\theta_0} = 300$ using $L_{x,W_S} = 100\theta_0$. The streamwise extent for obtaining a plateau in $C_{f,x}$ is $150\theta_0$, $165\theta_0$ and $40\theta_0$ (or, equivalently, $18\delta_0$, $8\delta_0$ and $5\delta_0$) for $Re_{\theta_0} = 300$, 600 and 900, respectively (note that $150\theta_0$ for $Re_{\theta_0} = 300$ has been obtained from the data using $L_{x,W_S} = 200\theta_0$ and $300\theta_0$ shown in § 3.1). Note that $C_{f,x}$ obtained from the LES of Kannepalli & Piomelli (2000) does not exhibit a plateau in the 3DTBL region, which seems to be due to the coarse streamwise spatial resolution in their simulation given that the agreement with the data for $Re_{\theta_0} = 600$ is excellent except for the 3DTBL region. The streamwise extent for $Re_{\theta_0} = 900$ (i.e. $5\delta_0$ or $40\theta_0$) is approximately half that of Lohmann (1976) in this spinning cylinder experiment. The reason for the difference is likely to be

because the imposition of W_S yields a 3DTBL more efficiently over a flat plate than over a spinning cylinder. With increasing W_S, the streamwise locations at which both $C_{f,x}$ and $C_{f,z}$ attain near-plateaus remain essentially unchanged, whereas the magnitudes for $W_S/U_0 = 2$ is greater than that for $W_S/U_0 = 1$ (see figure 14*b*,*d*) as observed in Lohmann's (1976) experiment. The increased magnitudes of $C_{f,x}$ and $C_{f,z}$ are intrinsically associated with the energized vortical structures, as will be discussed in § 5.3.

In the recovery region, the magnitude of $C_{f,x}$ tends to approach that of a 2DTBL when x/θ_0 reaches approximately 300. The Reynolds-number dependence of $C_{f,x}$ is also significant. In the latter context, Kannepalli & Piomelli (2000) used a power-law relation on the basis of a 1/7 power-law mean velocity in a 2DTBL, i.e.

$$C_{f,x} = 0.020 Re_{\delta}^{-1/6}, \tag{5.1}$$

(see (6-68) of White 1991), for estimating the Reynolds-number dependence (here Re_δ denotes the Reynolds number based on U_0 and δ_{99}). They noted that, if the experimental $C_{f,x}$ by Driver & Johnston (1990) is multiplied by $(Re_{\delta,exp}/Re_{\delta,LES})^{1/6}$, the resulting $C_{f,x}$ agrees well with the LES data of Kannepalli & Piomelli (2000). Close inspection of the present DNS data at $x/\theta_0 = 300$ has shown that, while the prediction of (5.1) is excellent for $Re_{\theta_0} = 300$, (5.1) underestimates $C_{f,x}$ by approximately 14 % for $Re_{\theta_0} = 900$. The latter result is attributed to the increased momentum thickness and Reynolds number in the 3DTBL and recovery regions owing to the effect of three-dimensionality (see figure 13*c*,*d*), whilst the boundary layer thickness remains invariably unchanged by cross-flow (the distribution is not shown here). Indeed, the power-law relation of Smits, Matheson & Joubert (1983), *viz.*

$$C_{f,x} = 0.024 Re_{\theta}^{-1/4}, \tag{5.2}$$

which predicts $C_{f,x}$ in a 2DTBL excellently over a wide range of Reynolds number (see Schlatter & Örlü 2010), leads to a better prediction of $C_{f,x}$ for $Re_{\theta_0} = 900$ in the recovery region (i.e. the difference between the DNS data and (5.2) is approximately 5 % for $Re_{\theta_0} = 900$ at $x/\theta_0 = 300$).

To examine the Re dependence of $C_{f,x}$ and $C_{f,z}$ further, figure 15 shows the distributions of inner-normalized viscous ($C_{f,x\,vis}$ and $C_{f,z\,vis}$) and turbulent ($C_{f,x\,turb}$ and $C_{f,z\,turb}$) parts in the mean energy balances (i.e. (4.2) and (4.5)) as a function of x/θ_0 for $Re_{\theta_0} = 300$, 600 and 900 with $W_S/U_0 = 1$. In the 2DTBL region ($0 \le x/\theta_0 \le 100$), $(2^{1/2}/C_f^{3/2})C_{f,x\,vis}$ remains essentially unchanged independently of the Reynolds number (figure 15*a*), whilst $(2^{1/2}/C_f^{3/2})C_{f,x\,turb}$ increases with increasing Reynolds number (figure 15*b*). This latter behaviour is consistent with the Re dependence in a 2-D flow by Renard & Deck (2016), Abe & Antonia (2016) and Wei (2018). In the 3DTBL region ($100 \le x/\theta_0 \le 200$), the magnitudes of both the viscous and turbulent parts decrease significantly due to the change of the surface shear-stress direction, and depend less on the Reynolds number at a downstream station of a 3DTBL. The latter Re independence is most likely due to the effect of the mean spanwise shear resulting from the imposition of W_S. For all three Reynolds numbers, the magnitude of $C_{f,z\,turb}$ is greater than that of $C_{f,x\,turb}$, which highlights that, in a 3DTBL, $\overline{uv}$ is less efficient in extracting energy from mean flow than $\overline{vw}$. Also, the increase in W_S yields less extraction of energy from $\overline{uv}$, while $C_{f,z\,turb}$ (i.e. the energy extracted from $\overline{vw}$) contributes almost exclusively to $C_{f\,turb}$ (the distributions for $W_S/U_0 = 2$ are not shown here). In the recovery region ($200 \le x/\theta_0 \le 400$), there is an increased magnitude of the turbulent part ($C_{f,x\,turb}$) for a larger Reynolds

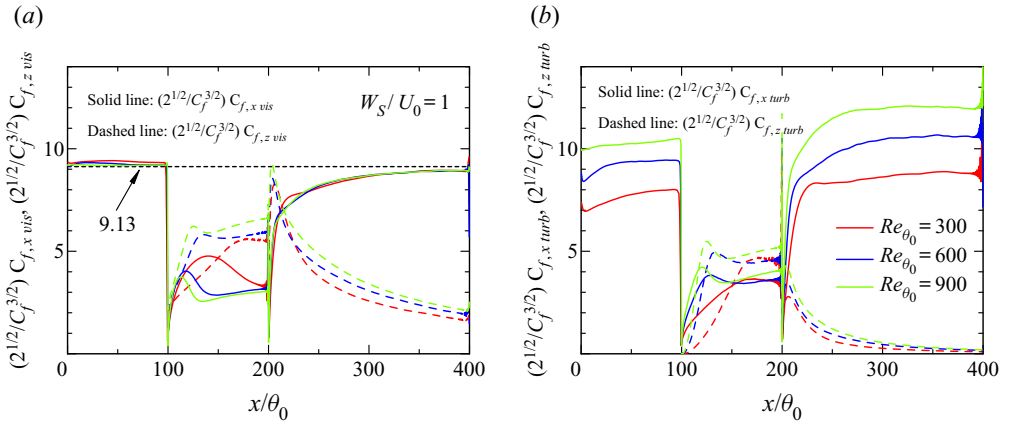

FIGURE 15. Distributions of terms on the right-hand side of (4.2) and (4.5) as functions of x/θ_0 for $Re_{\theta_0} = 300$, 600 and 900 with $W_S/U_0 = 1$: (*a*) $(2^{1/2}/C_f^{3/2})C_{f,x\,vis}$ and $(2^{1/2}/C_f^{3/2})C_{f,z\,vis}$; and (*b*) $(2^{1/2}/C_f^{3/2})C_{f,x\,turb}$ and $(2^{1/2}/C_f^{3/2})C_{f,z\,turb}$. The data shown have been obtained with $L_{x,W_S} = 100\theta_0$.

number (figure 15*b*). Also, non-zero values of $C_{f,z\,vis}$ and $C_{f,z\,turb}$ are observed for the three Reynolds numbers. These behaviours underline that the effect of three-dimensionality propagates into the recovery region. This point will be discussed further in § 5.5.

5.2. *Departure from the 'law of the wall' in a non-equilibrium 3DTBL*

Here, we discuss the 'law of the wall' in a non-equilibrium 3DTBL. In this context, the inner-layer scaling of the relative mean velocity (or, equivalently, the mean velocity magnitude), i.e.

$$Q_r \equiv (\overline{U}^2 + (\overline{W} - W_S)^2)^{1/2}, \tag{5.3}$$

has been intensively examined in a 3DTBL. There have been a number of observations indicating that the law of the wall, *viz.* (1.3), holds approximately in a shear-driven 3DTBL but with a larger magnitude of the von Kármán constant κ (see, for example, Bissonnette & Mellor 1974; Pierce & McAllister 1983; Moin *et al*. 1990) than $\kappa = 0.39$ in a 2DTBL (see Marusic *et al*. 2013). Given that the present 3DTBL will eventually approach the collateral state at a far-downstream station, the departure from the classical log law is intrinsically associated with a 3-D effect in a 3DTBL where there is a close relationship between a deficit of $\overline{U}$ and inviscid skewing (i.e. three-dimensionality) (see § 3.2).

Also, the classical inner scaling for the energy dissipation rate $\overline{\varepsilon}$ may be expressed as

$$\overline{\varepsilon}^+ \equiv \overline{\varepsilon}\nu/U_\tau^4 = 1/\kappa y^+. \tag{5.4}$$

In the latter context, Abe & Antonia (2016) made the matching argument to $\overline{\varepsilon}$ in a turbulent channel flow on the basis of the scaling arguments of Townsend (1976) (see § 8.8 of his book). They obtained the following relation by assuming that the Reynolds number is large enough to have a clear distinction between inner and outer regions, and there is a region

where the inner and outer scalings overlap, *viz.*

$$\overline{\varepsilon} y/U_\tau^3 = 1/\kappa_\varepsilon, \tag{5.5}$$

where κ_ε is a constant. In (5.5), the relevant length scale is the distance from the wall, y, to be distinguished unambiguously. Note that κ_ε is identical with κ when the Reynolds number is sufficiently large enough to establish the velocity log law, where the constant shear stress (i.e. $\tau \simeq \rho U_\tau^2$) and energy equilibrium (i.e. $P_k \simeq \overline{\varepsilon}$) assumptions also hold. Abe & Antonia (2016) noted that $\overline{\varepsilon} y/U_\tau^3$ approaches 2.54 (i.e. $1/\kappa_\varepsilon = 1/0.39$) in a channel, pipe and ZPG 2DTBL where the finite Re correction is required for a channel and a pipe due to the presence of the mean pressure gradient (see relations (4.22) and (4.23) of their paper).

Figure 16(*a*,*b*) shows the distributions of the inner-normalized mean velocity magnitude Q_r and energy dissipation rate $\overline{\varepsilon}$, respectively, with the semi-logarithmic coordinates, for $Re_{\theta_0} = 300$, 600 and 900 with $W_S/U_0 = 1.0$ and for $Re_{\theta_0} = 900$ with $W_S/U_0 = 2.0$ in a near-equilibrium 3DTBL ($x/\theta_0 = 175$). As the Reynolds number increases, the magnitude of $Q_r^+ (= Q_r/U_\tau)$ becomes smaller away from the wall than in a 2DTBL. For $Re_{\theta_0} = 900$, the velocity log law (i.e. (1.3)) tends to hold but with a larger magnitude of the von Kármán constant $\kappa = 0.44$, in particular, for a larger W_S, i.e. $W_S/U_0 = 2$ (see figure 16*a*), where the experimental data of Lohmann (1976) for $W_S/U_0 = 1.75$ agree reasonably well with the present distribution for Q_r^+ for $W_S/U_0 = 2.0$; the constant shear stress (i.e. $\tau \simeq \rho U_\tau^2$) and energy equilibrium (i.e. $P_k \simeq \overline{\varepsilon}$) assumptions also hold approximately for $Re_{\theta_0} = 900$ with $W_S/U_0 = 2.0$ (the distributions are not shown here). In the latter region, the production of k (i.e. $P_k \equiv -\overline{u_i u_j} S_{ij}$) shows a smaller magnitude than for a 2DTBL (see figure 16*c*) (note that $S_{ij} \equiv (\overline{U}_{i,j} + \overline{U}_{j,i})/2$), which indicates that the present 3DTBL is less efficient in extracting energy from the mean velocity than in a 2DTBL.

We also note that $\overline{\varepsilon}^+$ shows a better collapse for $y^+ > 20$ than Q_r^+, where (5.5) with $\kappa_\varepsilon = 0.44$ provides a good fit to the DNS data (see figure 16*b*,*d*). Indeed, an apparent plateau appears in the distribution of $\overline{\varepsilon} y/U_\tau^3$ in the region $y^+ = 20$ to $y/\delta_{99} = 0.15$ (see figure 16*d*). This underlines that the overlap scaling holds more clearly for small scales than for large scales. The constant value of $\overline{\varepsilon} y/U_\tau^3$ (i.e. (5.5)) is approximately 2.27, i.e. $1/\kappa_\varepsilon = 1/0.44$. Indeed, κ_ε is identical with κ when $Re_{\theta_0} = 900$. The implication at higher Reynolds number is that small scales are likely to lose the Re dependence more rapidly than large scales given a more distinct overlap scaling for $\overline{\varepsilon}$ than for $\overline{U}$; see also the DNS works in a turbulent channel flow by Abe & Antonia (2016, 2017), who noted that the overlap scaling for the energy and scalar dissipation rates is in fact established at a smaller value of Re_τ than that at which the mean velocity and scalar log laws hold. Also, the clear plateau of $\overline{\varepsilon} y/U_\tau^3$ (see the distribution in figure 16(*d*) for a larger W_S case) indicates self-similarity in small scales, which is intrinsically due to the mean spanwise shear arising from W_S. This point will be discussed further in the next subsection by focusing on the most energetic spanwise wavelengths of velocity fluctuations.

5.3. *Turbulence structures and energetic spanwise scales in a non-equilibrium 3DTBL*

In this subsection, we first discuss asymmetric turbulence structures observed in the present 3DTBL. Figure 17 shows the contours in the y–z plane of the instantaneous streamwise velocity fluctuation u together with those of a positive value of Q for the three Reynolds numbers in a near-equilibrium 3DTBL ($x/\theta_0 = 175$). As the Reynolds number increases, large-scale toppling u structures dominate in the outer region where the negative u structures preferentially correlate with the positive Q structures, the latter being

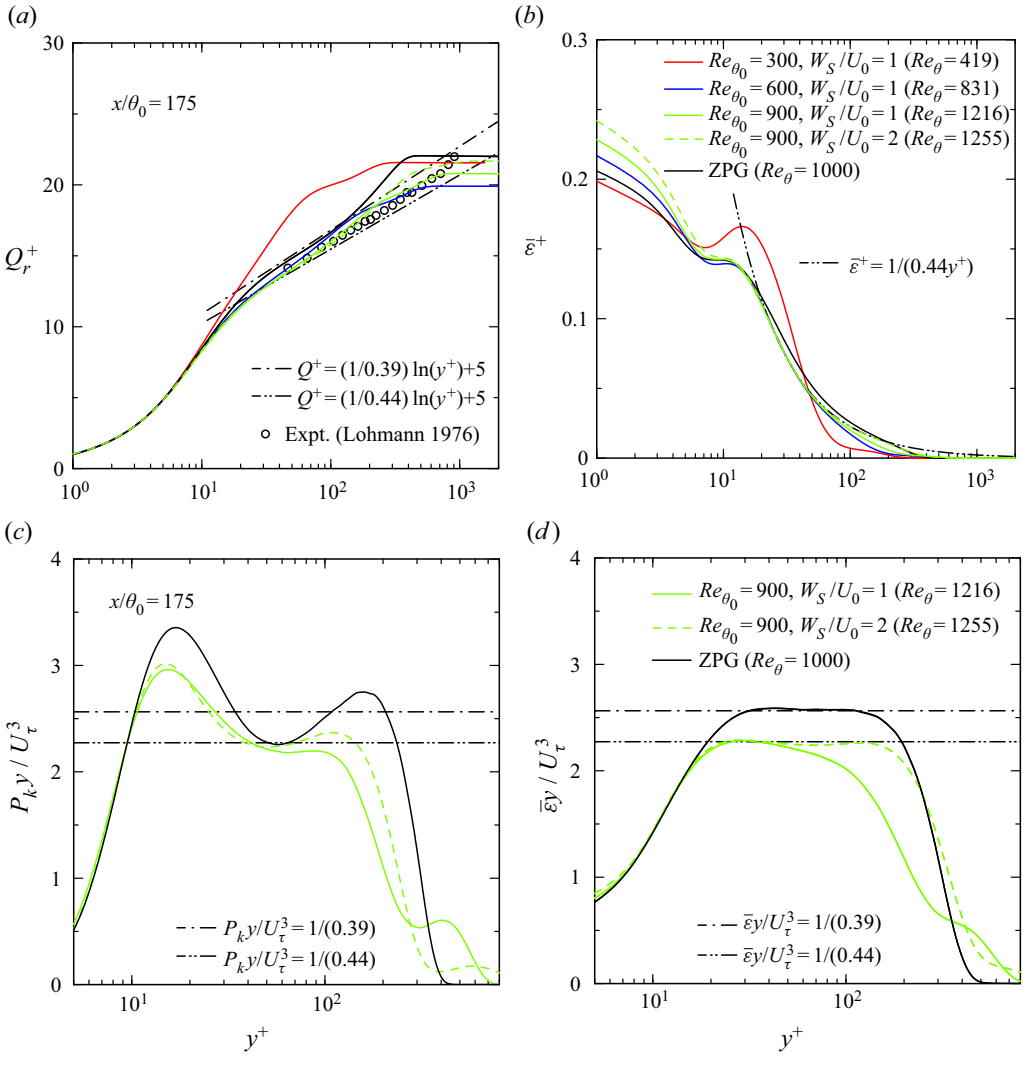

FIGURE 16. Distributions of Q_r^+, $\overline{\varepsilon}^+$, $P_k y/U_\tau^3$ and $\overline{\varepsilon} y/U_\tau^3$ in the 3DTBL region ($x/\theta_0 = 175$): (*a*) Q_r^+ for $Re_{\theta_0} = 300$, 600 and 900 with $W_S/U_0 = 1$ and for $Re_{\theta_0} = 900$ with $W_S/U_0 = 2$; (*b*) $\overline{\varepsilon}^+$ or $Re_{\theta_0} = 300$, 600 and 900 with $W_S/U_0 = 1$ and for $Re_{\theta_0} = 900$ with $W_S/U_0 = 2$; (*c*) $P_k y/U_\tau^3$ for $Re_{\theta_0} = 900$ with $W_S/U_0 = 1$ and 2; and (*d*) $\overline{\varepsilon} y/U_\tau^3$ for $Re_{\theta_0} = 900$ with $W_S/U_0 = 1$ and 2. The data shown have been obtained with $L_{x,W_S} = 100\theta_0$. Also plotted for comparison are the DNS data of a ZPG 2DTBL for $Re_\theta = 1000$ obtained in the present work.

stretched by cross-flow. Indeed, not only near-wall streaks but also outer-layer structures exhibit asymmetries due to the straining by cross-flow, which are reminiscent of the 'toppling structures' hypothesized by Bradshaw & Pontikos (1985). The energized vortical structures are intrinsically associated with the abruptly increased drag (figure 14). We note that, for the largest Re_{θ_0} with a large W_S (i.e. $Re_{\theta_0} = 900$ and $W_S/U_0 = 2$), both the u and Q structures are stretched significantly by cross-flow, showing asymmetries with approximately $-30°$ (see figure 17*d*). The asymmetric vortical structures are most likely associated with the excellent overlap scaling established for the energy dissipation rate

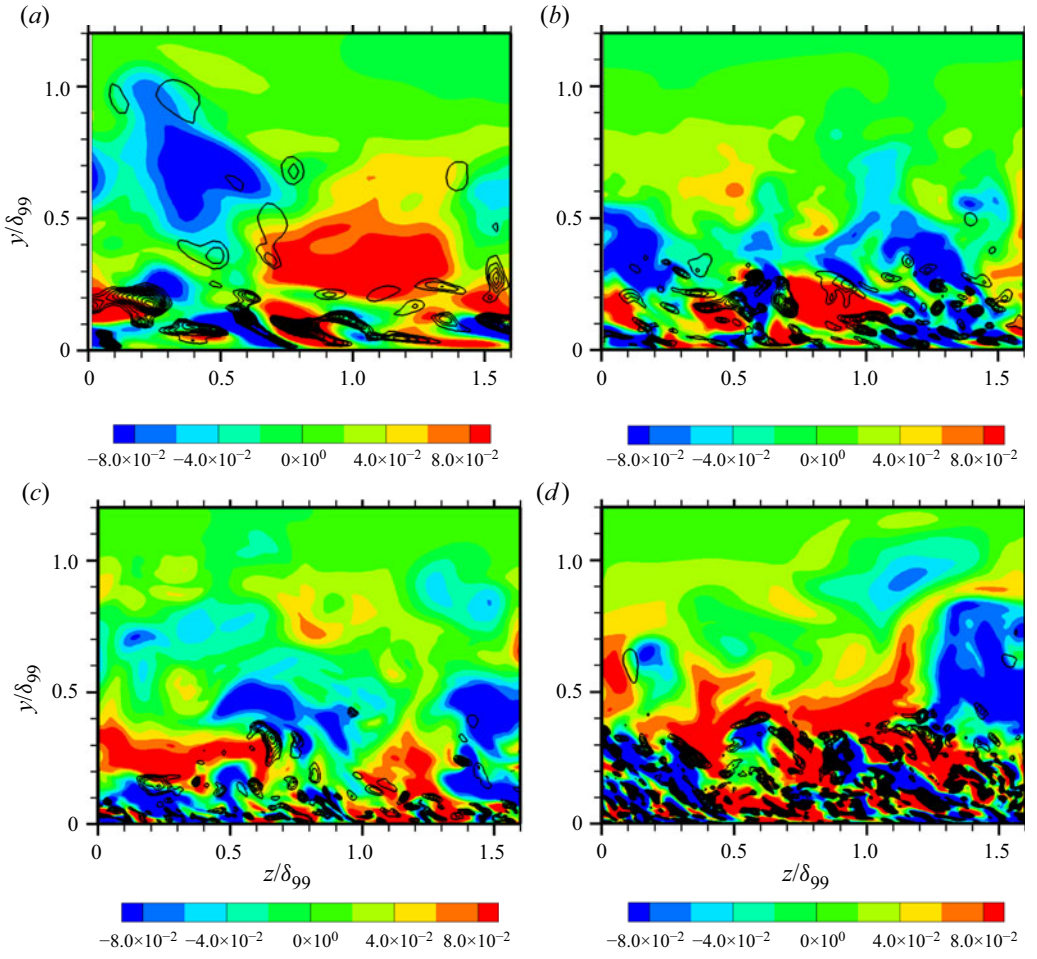

FIGURE 17. Contours in the y–z plane of u (colour) and a positive value of Q (line) in the 3DTBL region ($x/\theta_0 = 175$) for $Re_{\theta_0} = 300$, 600 and 900: (*a*) u/U_0 for $Re_{\theta_0} = 300$ with $W_S/U_0 = 1$; (*b*) u/U_0 for $Re_{\theta_0} = 600$ with $W_S/U_0 = 1$; (*c*) u/U_0 for $Re_{\theta_0} = 900$ with $W_S/U_0 = 1$; and (*d*) u/U_0 for $Re_{\theta_0} = 900$ with $W_S/U_0 = 2$. The data shown have been obtained with $L_{x,W_S} = 100\theta_0$.

$\overline{\varepsilon}$ (figure 16*d*). This figure also highlights an intrinsic difference between the shear-driven and pressure-driven 3DTBLs, i.e. both the near-wall and outer-layer structures are affected by cross-flow in the shear-driven 3DTBL, whilst the outer-layer structures are exclusively altered in the pressure-driven 3DTBL (see figure 5 of Schlatter & Brandt 2010).

In figure 17, we also see an interface between the 2-D and 3-D structures at $y/\delta_{99} = 0.3 \sim 0.4$ for all three Reynolds numbers, which indicates that there is a reduced interaction between the inner and outer regions due to inviscid skewing. A similar behaviour was observed in the recent experimental work of Kevin *et al.* (2019) in a 3DTBL with an angled ribbed surface. In this context, wall-normal two-point correlations, defined such that

$$R_{aa}(y_r, y) = \frac{\overline{a(y_r)a(y)}}{\overline{a(y_r)a(y_r)}}, \tag{5.6}$$

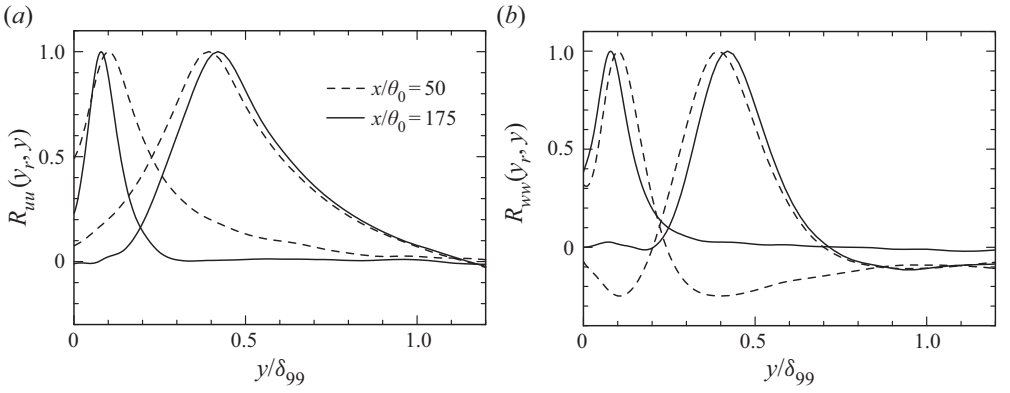

FIGURE 18. Wall-normal two-point correlations for $Re_{\theta_0} = 300$ with $W_S/U_0 = 1$: (*a*) $R_{uu}(y_r, y)$; and (*b*) $R_{ww}(y_r, y)$. The averaging is based on a time period $t^+ \approx 2332$. The data have been obtained in both the 2DTBL and 3DTBL regions ($x/\theta_0 = 50$ and 175) at two reference stations (i.e. $y_r/\delta_{99} \approx 0.1$ and 0.4). The data shown have been obtained with $L_{x,W_S} = 100\theta_0$.

where y_r is a reference y location and $a \equiv u$, v or w, have been examined. Figure 18 shows the distributions of $R_{uu}(y_r, y)$ and $R_{ww}(y_r, y)$ in the 2DTBL and 3DTBL regions ($x/\theta_0 = 50$ and 175) at two reference stations (i.e. $y_r/\delta_{99} \approx 0.1$ and 0.4). Note that, for this quantity, the data have been obtained for $Re_{\theta_0} = 300$ with $W_S/U_0 = 1$, using $L_{x,W_S} = 100\theta_0$; averaging is based on a time period of $t^+ \approx 2332$. This figure indicates that the u and w correlations in the 3DTBL region approach zero at a smaller separation than those in the 2-D region (a similar trend is observed for the v correlations (not shown here)). This result highlights that there is a reduced correlation of velocity fluctuations in the present 3DTBL.

It was also reported that in a 2DTBL (Hutchins & Marusic 2007) and a channel flow (Abe, Kawamura & Choi 2004), large-scale footprints exist in the near-wall region as a consequence of the interaction between the inner and outer regions. Footprints are, however, not observed clearly in the present 3DTBL, which is most likely due to the reduced interaction between the inner and outer regions (the instantaneous u contours in the x–z plane near a wall are not shown here).

To provide further statistical evidence regarding the reduced interaction, one-dimensional spanwise spectra, i.e.

$$\int_0^\infty \phi_{aa}(k_z)\,\mathrm{d}k_z = \int_0^\infty k_z\phi_{aa}(k_z)\,\mathrm{d}(\log k_z) = \overline{aa}, \tag{5.7}$$

have been investigated, where ϕ denotes the spectral density, k_z the spanwise wavenumber, $\lambda_z = 2\pi/k_z$ being the corresponding wavelengths, and $a \equiv u$, v or w. Figure 19(*a*,*b*) shows the $\lambda_z - y$ contours of the normalized premultiplied spanwise u spectra $k_z\phi_{uu}(k_z)$ (line) and uv co-spectra $k_z Co_{uv}(k_z)$ (colour) in the 2DTBL and 3DTBL regions ($x/\theta_0 = 50$ and 175). Note that the uv co-spectra denote the real part of the cross-spectra; the same dataset as for the wall-normal two-point correlations has been used for this spectral analysis. In the 2-D region, the global spectral mode is observed in the outer region for both the u spectra and the uv co-spectra at large λ_z ($\geq 0.6\delta_{99}$) where the correspondence between the two spectra is reasonably good (see figure 19*a*). This behaviour highlights that the large-scale u structures are active for transporting the momentum.

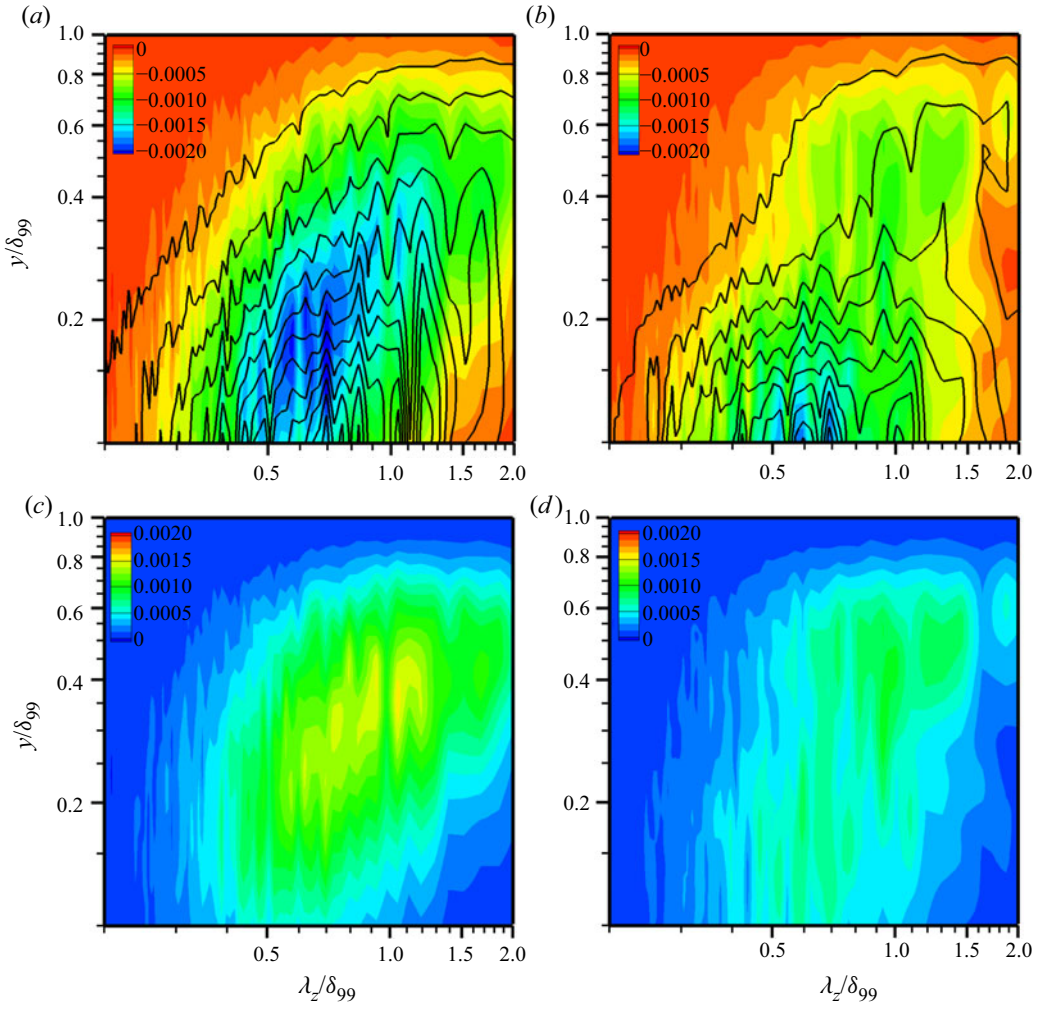

FIGURE 19. Contours in the $\lambda_z - y$ plane of normalized premultiplied spanwise u spectra $k_z\phi_{uu}(k_z)$, uv co-spectra $k_zCo_{uv}(k_z)$ and weighted uv co-spectra $-4k_z(\,y/\delta_{99})Co_{uv}(k_z)(1 - y/\delta_{99})$ in the 2DTBL and 3DTBL regions ($x/\theta_0 = 50$ and 175) for $Re_{\theta_0} = 300$ with $W_S/U_0 = 1$: (*a*) $k_z\phi_{uu}(k_z)/U_0^2$ (line) and $k_zCo_{uv}(k_z)/U_0^2$ (colour) at $x/\theta_0 = 50$; (*b*) $k_z\phi_{uu}(k_z)/U_0^2$ (line) and $k_zCo_{uv}(k_z)/U_0^2$ (colour) at $x/\theta_0 = 175$; (*c*) $-4k_z(\,y/\delta_{99})Co_{uv}(k_z)(1 - y/\delta_{99})/U_0^2$ at $x/\theta_0 = 50$; and (*d*) $-4k_z(\,y/\delta_{99})Co_{uv}(k_z)(1 - y/\delta_{99})/U_0^2$ at $x/\theta_0 = 175$. The averaging is based on a time period $t^+ \approx 2332$. The data shown have been obtained with $L_{x,W_S} = 100\theta_0$.

The global mode, however, becomes weakened in the 3-D region, indicating the reduced interaction between the inner and outer regions (see figure 19*b*) – note that the reduced spectral energy in the outer layer is also observed for the premultiplied spanwise v and w spectra, $k_z\phi_{vv}(k_z)$ and $k_z\phi_{ww}(k_z)$ (not shown here) in the 3DTBL region. In particular, we observe the decreased magnitude of $k_zCo_{uv}(k_z)/U_0^2$ at $y/\delta_{99} = 0.3 \sim 0.4$ in the 3DTBL region, consistent with the reduced magnitude of $-\overline{uv}$ in the outer region. This reduced $k_z\phi_{uu}(k_z)/U_0^2$ is intrinsically associated with a smaller magnitude of $C_{f,x\,turb}$ than in the collateral state and thus the lower efficiency in extracting energy from the mean flow (see § 4.1).

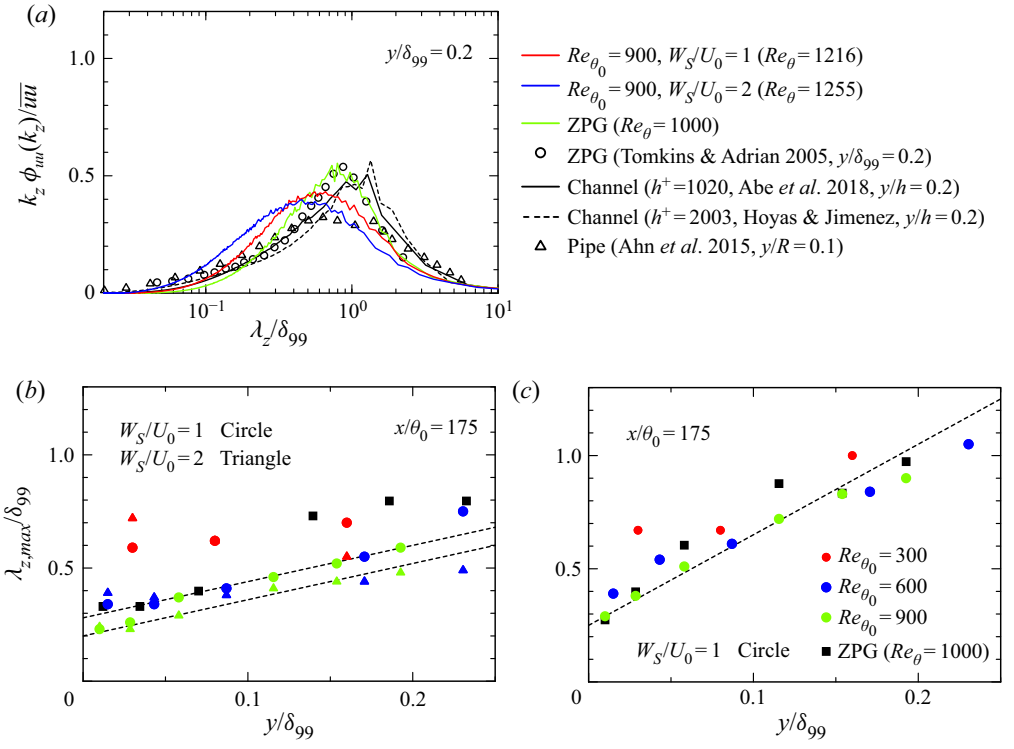

FIGURE 20. One-dimensional premultiplied spanwise u spectra at $y/\delta_{99}=0.2$ of a 3DTBL and the most energetic spanwise scales, $\lambda_{z,max}$, obtained from peaks of premultiplied spanwise spectra below $y/\delta_{99}=0.2$: (*a*) $k_z\phi_{uu}\,(k_z)\,/\overline{uu}$ for $Re_{\theta_0}=900$ with $W_S/U_0=1$ and 2; (*b*) $\lambda_{z,max}/\delta_{99}$ for u for $Re_{\theta_0}=300$, 600 and 900 with $W_S/U_0=1$ and 2; and (*c*) $\lambda_{z,max}/\delta_{99}$ for w for $Re_{\theta_0}=300$, 600 and 900 with $W_S/U_0=1$. In (*a*), the spectra are compared with those in a turbulent channel flow of Abe *et al.* (2018) (black solid line) and Hoyas & Jiménez (2008) (black dashed line) for $h^+=1020$ and 2003 at $y/h=0.2$, respectively. Also included are the spectra of Tomkins & Adrian (2005) in a ZPG TBL for $\delta^+=2216$ at $y/\delta=0.2$ (circle) and those of Ahn *et al.* (2015) in a turbulent pipe for $R^+=3008$ at $y/R=0.1$ (triangle). In (*b*,*c*), the dashed lines denote the linear fittings. In (*a–c*), the data shown have been obtained with $L_{x,W_S}=100\theta_0$.

In the latter context, it would also be instructive to pay attention to the spectral analysis by Deck *et al.* (2014), who discussed how $C_{f,x}$ in a 2DTBL is related to the spatial changes in turbulence motions. They focused on the contribution of the $\overline{uv}$ term to $C_{f,x}$ in the FIK identity (Fukagata *et al.* 2002), and examined the streamwise weighted uv co-spectra, i.e. $-4k_x(y/\delta_{99})Co_{uv}(k_x)(1-y/\delta_{99})$. Note that k_x denotes the streamwise wavenumber; the factor of (y/δ_{99}) arises from the $\overline{uv}$ term in the FIK identity. Deck *et al.* (2014) noted that in a 2DTBL, large scales in the outer region make a major contribution to $C_{f,x}$. A similar inspection has been made for the present spanwise weighted spectra, i.e. $-4k_z(y/\delta_{99})Co_{uv}(k_z)(1-y/\delta_{99})$ (see figure 19*c*,*d*), which display an outer energetic mode more clearly than $k_zCo_{uv}(k_z)$ (see figure 19*a*,*b*) in both the 2DTBL and 3DTBL regions. Also, we see in figure 19(*c*,*d*) that the weighted co-spectra in a 3DTBL exhibit a decreased magnitude of the global energetic mode at large λ_z ($\geq 0.6\delta_{99}$) compared with those in a 2DTBL. This result underlines the close relationship between the reduced $C_{f,x}$ and the decreased interaction between the inner and outer regions in the 3DTBL region.

We next quantify the spanwise organization of the u structures in a 3DTBL with the use of the energy spectra. Figure 20(a) shows the spanwise spectral density of u, $k_z\phi_{uu}(k_z)$, normalized by $\overline{uu}$, at $y/\delta_{99} \approx 0.2$, compared with those in a 2DTBL (present DNS; Tomkins & Adrian 2005), channel flow (Hoyas & Jiménez 2008; Abe *et al*. 2018) and pipe flow (Ahn *et al*. 2015). Abe *et al*. (2018) noted that, while the outer flow is completely different between the internal and external flows (e.g. the presence of the $\lambda_z/h = 1.3$–1.6 or $\lambda_z/R = 1.3$ mode in the internal flows, where R denotes the pipe radius), there is some similarity in the spectral peak at a lower wavelength ($\lambda_z/h = 0.8$–0.9 (channel), $\lambda_z/R = 0.7$ (pipe) and $\lambda_z/\delta_{99} = 0.8$ (boundary layer)). They associated this similarity with the fact that the magnitude of the von Kármán constant κ does not differ significantly between the three flows and is approximately 0.39 at extremely large Reynolds number (Marusic *et al*. 2013). Figure 20(a) highlights that the peak wavelength of $k_z\phi_{uu}(k_z)$ in a 3DTBL appears at a shorter wavelength than that in a 2DTBL, due to the turning of large-scale u structures by inviscid skewing (see figure 21, where the contours in the x–z plane of the instantaneous streamwise and spanwise velocity fluctuations, u and w, are shown for $Re_{\theta_0} = 900$ with $W_S/U_0 = 1$ and 2 together with those in a 2DTBL).

We now examine the most energetic spanwise scales of the asymmetric u structures, $\lambda_{z,max}$, by plotting the peak wavelengths of the premultiplied spectra $k_z\phi_{uu}(k_z)$ below $y/\delta_{99} \approx 0.2$ in figure 20(b). Also plotted in figure 20(c) is the distribution of $\lambda_{z,max}$ for w for comparison. Note that the peak wavelength of the premultiplied spectrum corresponds to the most energetic scale contributing to the mean-square value; a least-squares fitting has been made for the spectral peak to obtain $\lambda_{z,max}$. While the self-similar behaviour is not observed clearly in a 2DTBL due to the effect of large scales (see Jiménez & Hoyas 2008; Abe *et al*. 2018), the linear increase in $\lambda_{z,max}$ is indeed observed for the u spectra in a 3DTBL below $y/\delta_{99} = 0.2$ for both $W_S/U_0 = 1$ and 2. Note that in a 3DTBL, there is also a linear increase in $\lambda_{z,max}$ for the w spectra with $W_S/U_0 = 1$ (figure 20c), but not with $W_S/U_0 = 2$ (not shown here) due to the presence of large-scale elongated w structures (see figure 21f).

Given the notion of Nickels *et al*. (2007) that any eddy with a size that scales with its distance from the wall may be considered to be attached to the wall, the well-established linear dependence of $\lambda_{z,max}$ for u in a 3DTBL is intrinsically associated with the attached-eddy hypothesis of Townsend (1976). Inspection of the instantaneous u contours in the x–z plane (figure 21a,c,e) indicates that large-scale u structures become less anisotropic with increasing W_S. These results underline that the spanwise mean shear resulting from the imposition of W_S yields a self-similar behaviour in the asymmetric u structures. The departure from self-similarity due to the large-scale contamination was indeed reported in a turbulent channel flow by Jiménez & Hoyas (2008), Hwang (2015) and Abe, Antonia & Toh (2018). Note that, while some u structure are aligned with the shear-stress direction in the collateral state (i.e. $\alpha = -45^\circ$ and -60°) (see the black solid lines in figure 21c–f), most of the u structures are altered slowly compared with the w structures. This slow turning of the u structures is most likely associated with the slower approach to the collateral state for $\overline{U}$ than $\overline{W}$. We also note that $\lambda_{z,max}$ for w also shows a linear increase with respect to y for $W_S/U_0 = 1$, but not for $W_S/U_0 = 2$ (see figure 20c) since large scales dominate for w for a larger W_S (see figure 21f).

As for vortical structures in a 2DTBL, Adrian, Meinhart & Tomkins (2000) reported hairpin vortical structures and noted the relationship with the negative u structures. In the present 3DTBL, Kiesow & Plesniak (2003) hypothesized skewing of hairpin vortices. Inspection of the contours in the x–y plane (not shown) and x–z plane (figure 21) has revealed that, as observed in a 2DTBL by Adrian *et al*. (2000), the low-momentum regions preferentially correlate with vortical structures. With increasing W_S, the correlation

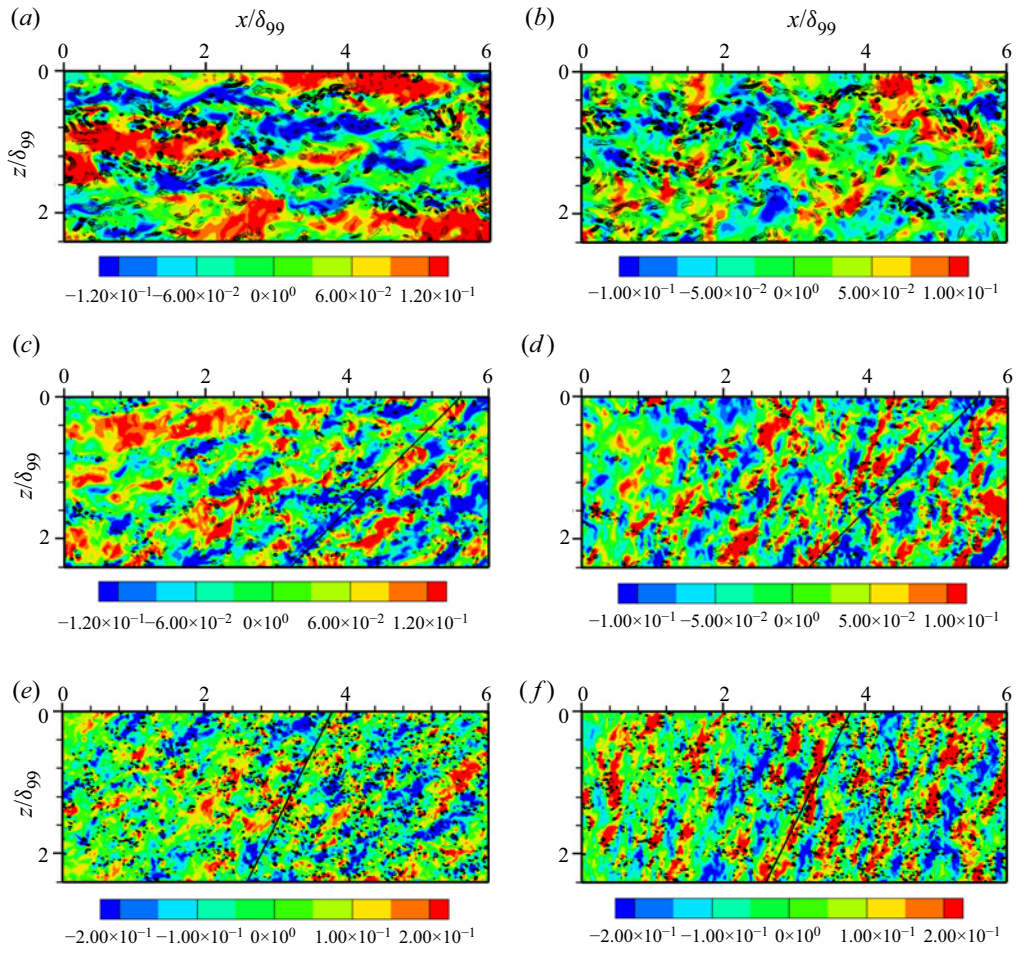

FIGURE 21. Contours in the x–z plane of u (colour) (a,c,e) and w (colour) (b,d,f) together with those of a positive value of Q (line) in 2DTBLs and 3DTBLs: (a) u/U_0 in a 2DTBL for $Re_\theta \approx 1000$; (b) w/U_0 in a 2DTBL for $Re_\theta \approx 1000$; (c) u/U_0 in a 3DTBL for $Re_{\theta_0} = 900$ with $W_S/U_0 = 1$; (d) w/U_0 in a 3DTBL for $Re_{\theta_0} = 900$ with $W_S/U_0 = 1$; (e) u/U_0 in a 3DTBL for $Re_{\theta_0} = 900$ with $W_S/U_0 = 2$; and (f) w/U_0 in a 3DTBL for $Re_{\theta_0} = 900$ with $W_S/U_0 = 2$. In (c–f), structures in the 3DTBL region have been visualized with an enlarged view; the data shown in these panels have been obtained with $L_{x,W_S} = 100\theta_0$. In (c,d) and (e,f), the solid lines denotes the direction of $\alpha = -45^\circ$ and -60°, respectively, which correspond to the surface shear-stress direction in the collateral state.

between the u structures and vortical structures becomes weaker due to the breakdown of large-scale u structures (figure 21c,e). On the other hand, the w structures tend to exhibit elongated structures in the shear-stress direction (see also the black solid line in figure 21f) where vortical structures are aligned with the w structures (figure 21d,f). Indeed, the vortical structures change their directions due to inviscid skewing.

5.4. *Behaviour of the primary Reynolds shear stress $\overline{uv}$ in a non-equilibrium 3DTBL*

Recently, Lozano-Durán *et al*. (2020) discussed the reduced behaviour of the primary Reynolds shear stress $\overline{uv}$ in their 3-D channel DNS with a sudden imposition of mean

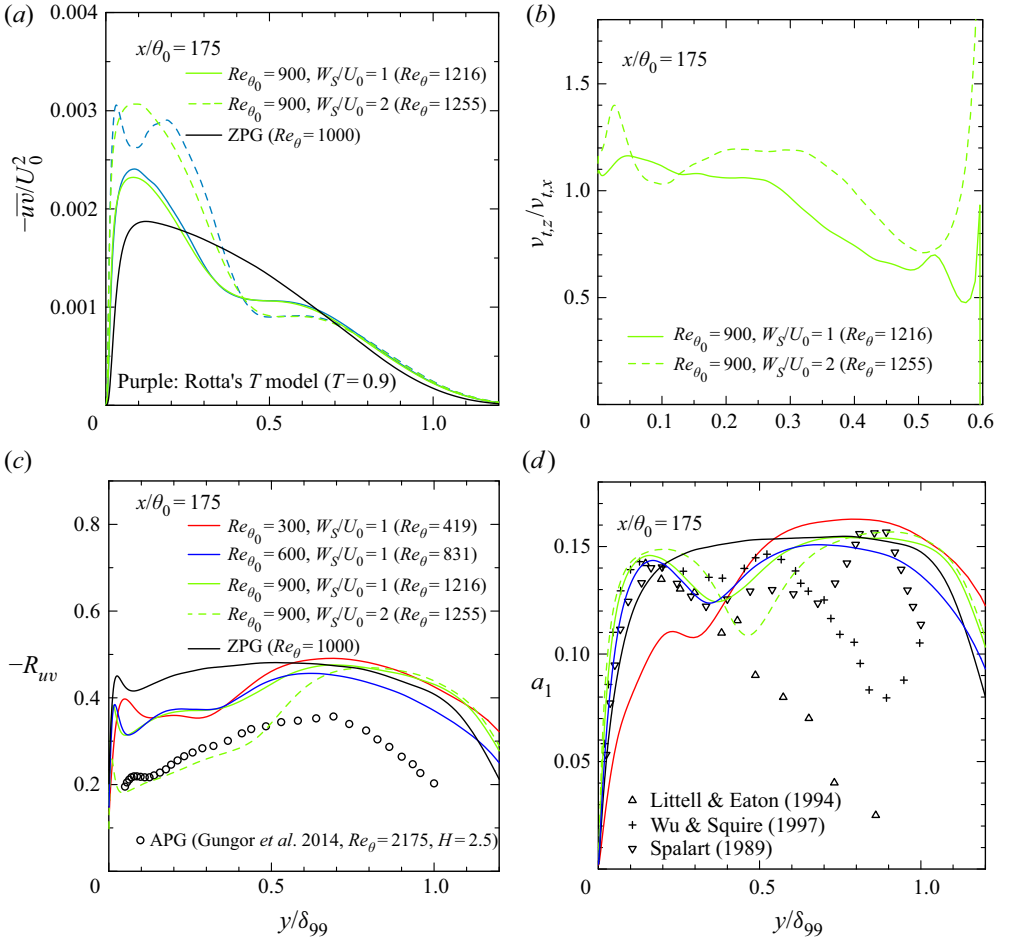

FIGURE 22. Distributions of the outer-normalized $-\overline{uv}$, the correlation coefficient $-R_{uv}$, the turbulent eddy viscosity ratio $\nu_{t,z}/\nu_{t,x}$ and the structure parameter a_1 in the 3DTBL region ($x/\theta_0 = 175$): (*a*) $-\overline{uv}/U_0^2$ for $Re_{\theta_0} = 900$ with $W_S/U_0 = 1$ and 2; (*b*) $\nu_{t,z}/\nu_{t,x}$ for $Re_{\theta_0} = 900$ with $W_S/U_0 = 1$ and 2; (*c*) $-R_{uv}$ for $Re_{\theta_0} = 300$, 600 and 900 with $W_S/U_0 = 1$ and $Re_{\theta_0} = 900$ with $W_S/U_0 = 2$; and (*d*) a_1 for $Re_{\theta_0} = 300$, 600 and 900 with $W_S/U_0 = 1$ and $Re_{\theta_0} = 900$ with $W_S/U_0 = 2$. The data shown have been obtained with $L_{x,W_S} = 100\theta_0$. Also plotted for comparison are the DNS data of a ZPG 2DTBL for $Re_\theta = 1000$ obtained in the present work.

spanwise pressure gradient. They explained it as a non-equilibrium effect rather than three-dimensionality. Here, we examine the behaviour of $\overline{uv}$ in the present 3DTBL and the implication for turbulence modelling.

Figure 22(*a*) shows the distributions of $\overline{uv}$, respectively, at a downstream station of the 3DTBL region ($x/\theta_0 = 175$) for $Re_{\theta_0} = 900$ with $W_S/U_0 = 1$ and 2. The magnitude of $-\overline{uv}/U_0^2$ in the inner region ($y/\delta_{99} \leq 0.2$) is increased significantly with cross-flow, whereas there is a reduced magnitude of $-\overline{uv}/U_0^2$ in the outer region. The latter decrease is also observed in the recent experiment by Kevin *et al.* (2019) in their 3DTBL on a ribbed surface. Close inspection of the instantaneous product uv (not shown here) shows a decrease in magnitude at the interface between the 2-D and 3-D structures (see figure 17

where the u contours in the y–z plane are shown), which supports the hypothesis of Bradshaw & Pontikos (1985) that rapid decreases of shear stress are caused by the sideways tilting of the large eddies away from their preferred orientation. In the uv co-spectra (see figure 19), we also see the statistical evidence on a decreased global mode at large λ_z ($\geq 0.6\delta_{99}$) in the 3DTBL region. These results indicate that the reduction in $\overline{uv}/U_0^2$ in the present shear-driven flow is intrinsically associated with a reduced interaction between the inner and outer regions due to inviscid skewing. Inspection of figure 22(a) has revealed that the relative reduction of $\overline{uv}/U_0^2$ (i.e. the dip at $y/\delta_{99} \approx 0.4$) to the value of a 2DTBL is approximately 25 %, the latter value being identical with the result of Lozano-Durán *et al.* (2020) in the 3-D channel DNS. In the latter DNS, a mean spanwise pressure gradient is imposed, which is equivalent to applying a spanwise motion to the walls, in the opposite directions (this was pointed out by Dr G. N. Coleman, private communication 2019). There is thus a similarity between the present 3DTBL and that of Lozano-Durán *et al.* (2020). In both 3DTBLs, the mean streamwise vorticity $\overline{\Omega}_x$ propagates from the near-wall region to the outer layer. Also, a self-similar behaviour is observed. Given these similarities, a non-equilibrium effect reported by Lozano-Durán *et al.* (2020) may involve a reduced interaction between the inner and outer regions due to three-dimensionality.

At this x station ($x/\theta_0 = 175$), there appear a deficit of $\overline{U}$ (not shown here) and also a decreased magnitude of the correlation coefficient $-R_{uv}(= -\overline{uv}/u_{rms}v_{rms})$ as in the APG TBL (see figure 22c where the present $-R_{uv}$ is nearly identical with that of Gungor *et al.* (2014) in a strong APG 2DTBL; see also figure 11 from Abe (2019)). This result, however, does not imply the similarity between the present 3DTBL and APG 2DTBL. Figure 22(d) shows the distributions of the structure parameter a_1 in the 3DTBL region ($x/\theta_0 = 175$). This figure highlights that the present magnitude attains $a_1 \approx 0.14$ at $y/\delta_{99} \approx 0.1$ where there is a maximum streamwise mean velocity deficit (the distribution of $\overline{U}$ is not shown here). The present value of $a_1(\approx 0.14)$ is greater than $a_1 = 0.11$ in the APG TBL by Spalart & Watmuff (1993). This result supports the finding of Coleman *et al.* (2000) that the impact of the APG on the outer-layer structure is more pronounced than that of the mean three-dimensionality. Also, the present distribution of a_1 in the inner region of a 3DTBL ($y/\delta_{99} \leq 0.2$) agrees well with the experimental results of Littell & Eaton (1994) in the rotating disk and the DNS and LES results of Spalart (1989) and Wu & Squires (1997) in the equilibrium 3DTBL (see figure 22d).

On the other hand, as for $\overline{uv}/U_0^2$, the significant decrease in magnitude of a_1 is observed in the present 3DTBL, as in a 'pressure-driven' skewed TBL by Anderson & Eaton (1989). This supports the notion of Eaton (1995) that the reduction of the Reynolds shear stress by the mean flow three-dimensionality is a common feature in 3DTBLs. Note that the reduction is also observed in the Reynolds normal stresses in the outer region – see figure 23(c,d) where the present DNS data for $\overline{uu}/U_0^2$ and $\overline{vv}/U_0^2$ agree well with the experiment by Kiesow & Plesniak (2003). As noted by Kiesow & Plesniak (2003), the near-wall Reynolds normal stresses, normalized by U_0^2, increase with the magnitude of cross-flow (the distribution of $\overline{ww}/U_0^2$ is not shown here). In particular, the two wall-parallel inactive motions (i.e. $\overline{uu}/U_0^2$ and $\overline{ww}/U_0^2$) increase significantly with W_S. For all three Reynolds numbers (i.e. $Re_{\theta_0} = 300$, 600 and 900), the energy redistribution between the Reynolds normal stresses is also altered when $W_S/U_0 = 2$, i.e. the energy redistributes from $\overline{ww}$ to $\overline{uu}$ away from the wall independently of the Reynolds number (the distributions of the pressure strain for $Re_{\theta_0} = 600$ and 900 are not shown here).

We now discuss the implication of the reduced $\overline{uv}$ for the turbulence modelling. The reduced magnitude of $\overline{uv}$ (figure 22a) implies a lag between the Reynolds stress vector and the mean strain-rate one, which is intrinsically linked to the anisotropy of the turbulent

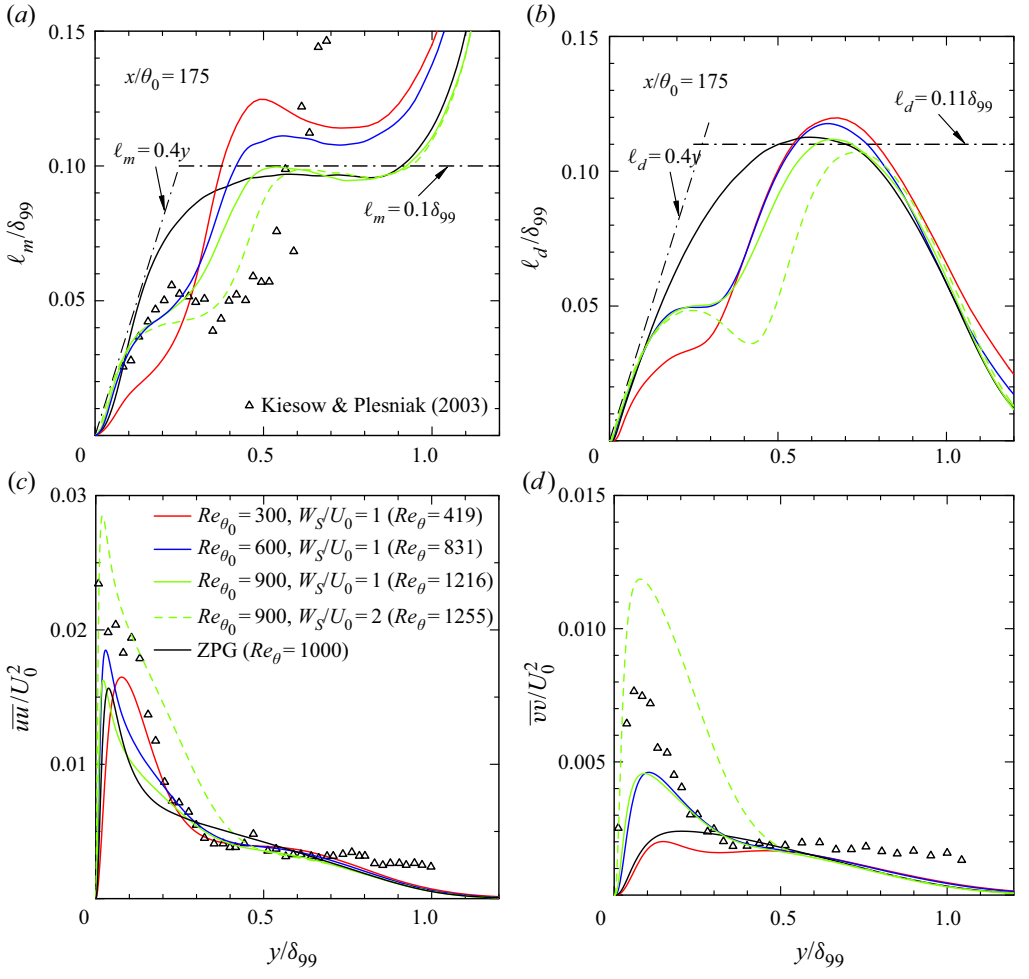

FIGURE 23. Distributions of the normalized mixing and dissipation lengths (ℓ_m and ℓ_d) and Reynolds normal stresses in the 3DTBL region ($x/\theta_0 = 175$) for $Re_{\theta_0} = 300$, 600 and 900 with $W_S/U_0 = 1$ and for $Re_{\theta_0} = 900$ with $W_S/U_0 = 2$: (*a*) ℓ_m/δ_{99}; (*b*) ℓ_d/δ_{99}; (*c*) $\overline{uu}/U_0^2$; and (*d*) $\overline{vv}/U_0^2$. In (*c*,*d*), the triangle denotes the experimental data of Kiesow & Plesniak (2003) for $Re_\theta = 1450$. The data shown have been obtained with $L_{x,W_S} = 100\theta_0$. Also plotted for comparison are the DNS data of a ZPG 2DTBL for $Re_\theta = 1000$ obtained in the present work.

eddy viscosity (see Anderson & Eaton 1989; Óelcmen & Simpson 1995; Johnston & Flack 1996). The ratio of the spanwise eddy viscosity,

$$\nu_{t,z} = -\overline{vw}/(\partial \overline{W}/\partial y), \tag{5.8}$$

to the streamwise eddy viscosity,

$$\nu_{t,x} = -\overline{uv}/(\partial \overline{U}/\partial y), \tag{5.9}$$

has been intensively examined in 3DTBLs, where the magnitude is often below unity (see Anderson & Eaton 1989; Óelcmen & Simpson 1995; Johnston & Flack 1996). Figure 22(*b*)

demonstrates that the present magnitude of $\nu_{t,z}/\nu_{t,x}$ is indeed below unity in the outer region of a near-equilibrium 3DTBL and decreases down to 0.6 at $y/\delta_{99} = 0.4 \sim 0.5$ since $\overline{vw} > \overline{uv}$ there.

On the other hand, the magnitude of $\nu_{t,z}/\nu_{t,x}$ is greater than unity in the inner region of a 3DTBL. These behaviours highlight the anisotropy of the turbulent eddy viscosity in the present non-equilibrium 3DTBL. In this context, Rotta (1979) introduced an empirical parameter T (being identical with the ratio $\nu_{t,z}/\nu_{t,x}$) into a mixing length model for predicting a non-equilibrium 3DTBL. While his model is not Galilean-invariant, it indeed provides an improved prediction (see Anderson & Eaton 1989; Óelcmen & Simpson 1993). In Rotta's (1979) model, the primary Reynolds shear stress is calculated such that

$$-\overline{uv} = \nu_{t,xx}(\partial\overline{U}/\partial y) + \nu_{t,xz}(\partial\overline{W}/\partial y), \tag{5.10}$$

where two anisotropic forms of the turbulent eddy viscosity, i.e.

$$\nu_{t,xx} = \nu_t(\overline{U}^2 + T\overline{W}^2)/Q_r^2 \tag{5.11}$$

and

$$\nu_{t,xz} = \nu_t(1-T)\overline{U}\,\overline{W}/Q_r^2, \tag{5.12}$$

are used. Here, we test Rotta's T model for the present 3DTBL by inserting the current DNS datasets into the right-hand sides of (5.10)–(5.12). Note that in (5.11) and (5.12), the effective turbulent eddy viscosity $\nu_t = -\overline{u_iu_j}S_{ij}/2S_{kl}S_{kl}$ (Spalart & Strelets 2000) is used, which is a coordinate-invariant form and can be described as a least-squares fit to the Reynolds stress tensor. The optimal value of T differs in different flows (see Anderson & Eaton 1989; Óelcmen & Simpson 1993). In the present study, $T = 0.9$ is used for yielding the closest prediction to the DNS data. Indeed, the calculated $\overline{uv}$ agrees reasonably well with the DNS data in the present flow (see figure 22*a*), which indicates that the effect of three-dimensionality (i.e. the Reynolds stress lags behind the mean strain) cannot be dismissed when predicting the present flow.

Also, the mixing length ℓ_m for a 3DTBL may be obtained as

$$\ell_m = (\overline{vw}^2 + \overline{uv}^2)^{1/4} \Bigg/ \left[\left(\frac{\partial\overline{U}}{\partial y}\right)^2 + \left(\frac{\partial\overline{W}}{\partial y}\right)^2\right]^{1/2} \tag{5.13}$$

(see Rotta 1979; Bradshaw 1987), which is a coordinate-invariant form. Figure 23(*a*) shows the distributions of normalized ℓ_m in the 3DTBL region ($x/\theta_0 = 175$). Clearly, the distributions follow the relation $\ell_m \approx 0.4y$ in the inner region ($y/\delta_{99} \leq 0.1$), whereas the magnitudes are reduced significantly in the outer region (i.e. $0.1 \leq y/\delta_{99} \leq 0.6$) and the latter are below the value of a 2DTBL (i.e. $\ell_m/\delta_{99} \approx 0.1$). This result also agrees reasonably well with the PIV measurement by Kiesow & Plesniak (2003) in the present flow (see figure 23*a*). A similar decrease is observed in the dissipation length scale, *viz.*

$$\ell_d = (\overline{vw}^2 + \overline{uv}^2)^{3/2}/\overline{\varepsilon} \tag{5.14}$$

(see figure 23*b*). This result is not surprising given that a near-energy-equilibrium condition (i.e. $P_k \simeq \overline{\varepsilon}$) is satisfied approximately there (the distribution is not shown here). These results indicate that the effect of three-dimensionality dominates in the 3DTBL region, which has an important implication for turbulence modelling, *viz.* the length scale reduction needs to be taken into account when developing a turbulence model for a 3DTBL given that the turbulent eddy viscosity is represented by $\nu_t \propto k^{1/2}\ell$.

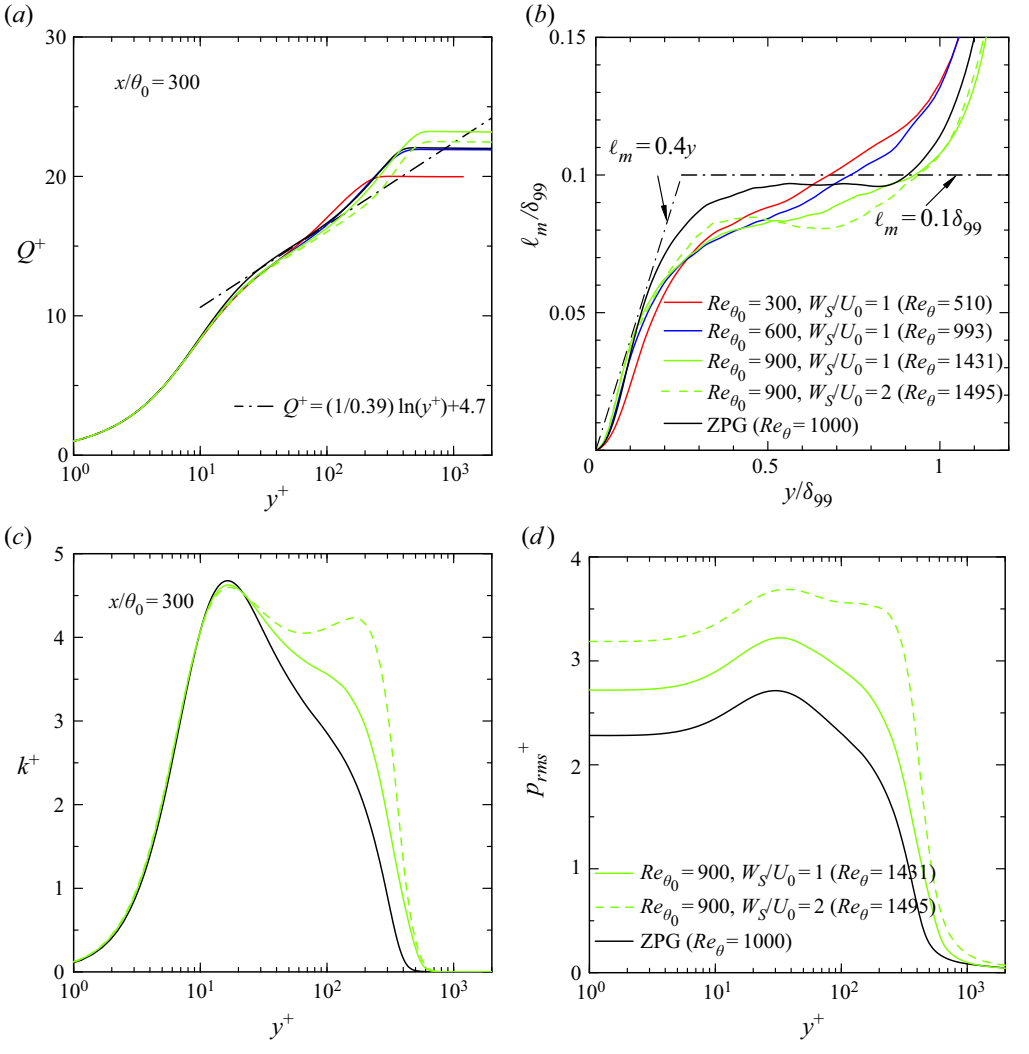

FIGURE 24. Distributions of the normalized Q_r, ℓ_m, k, p_{rms} in the recovery region ($x/\theta_0 = 300$): (*a*) Q_r^+ for $Re_{\theta_0} = 300$, 600 and 900 with $W_S/U_0 = 1$ and $Re_{\theta_0} = 900$ with $W_S/U_0 = 2$; (*b*) ℓ_m/δ_{99} for $Re_{\theta_0} = 300$, 600 and 900 with $W_S/U_0 = 1$ and for $Re_{\theta_0} = 900$ with $W_S/U_0 = 2$; (*c*) k^+ for $Re_{\theta_0} = 900$ with $W_S/U_0 = 1$ and 2; and (*d*) p_{rms}^+ for $Re_{\theta_0} = 900$ with $W_S/U_0 = 1$ and 2. The data shown have been obtained with $L_{x,W_S} = 100\theta_0$. Also plotted for comparison are the DNS data of a ZPG 2DTBL for $Re_\theta = 1000$ obtained in the present work.

5.5. *Recovery to a 2DTBL*

Finally, we discuss the recovery of a 3DTBL to a normal 2DTBL in light of the seminal work of Antonia & Luxton (1971) on a sudden change of a surface condition given the presence of the internal boundary layer (i.e. after turning off W_S, a new boundary layer develops inside a 3DTBL).

Figure 24 shows the distributions of the inner-normalized Q_r for $Re_{\theta_0} = 300$, 600 and 900 with $W_S/U_0 = 1$ and for $Re_{\theta_0} = 900$ with $W_S/U_0 = 2$ at a downstream station of the recovery region ($x/\theta_0 = 300$) in which the spanwise friction coefficient becomes negligibly small (figure 14*c*,*d*). While the near-wall distributions become closer to those

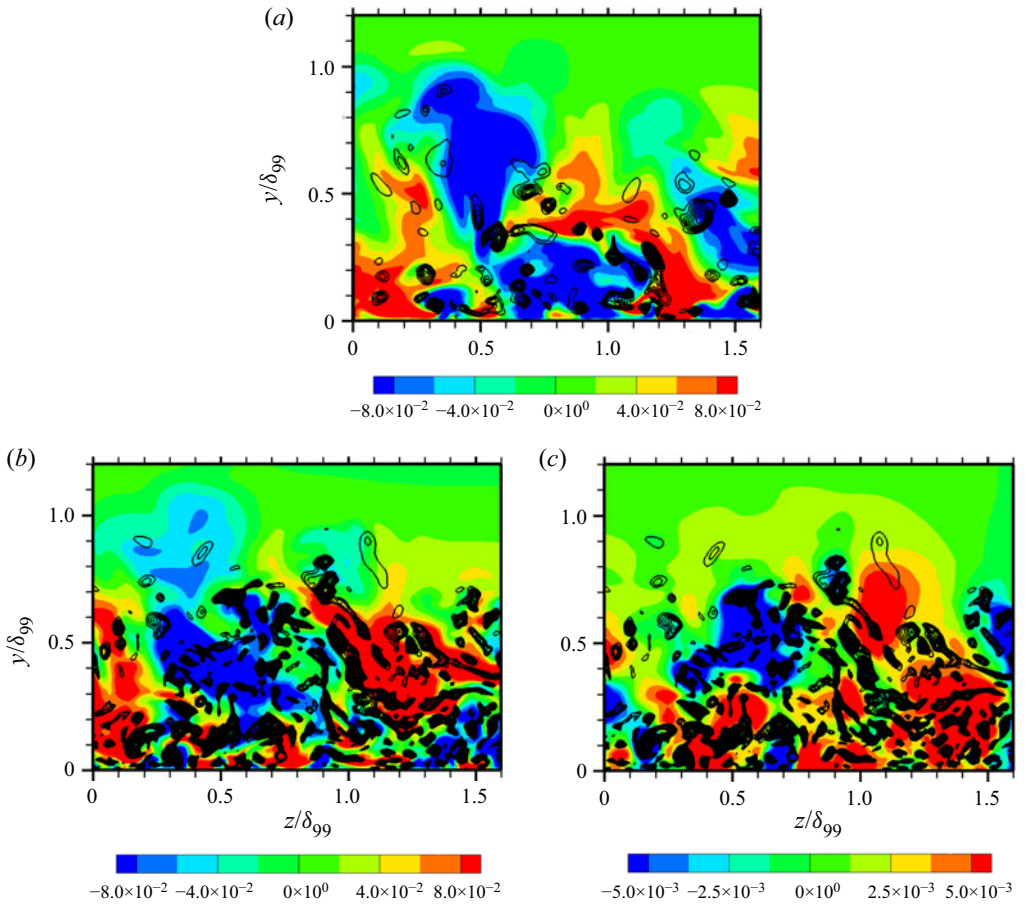

FIGURE 25. Contours in the y–z plane of u and p (colour) and a positive value of Q (line) in the recovery region compared with those in a ZPG 2DTBL: (*a*) u/U_0 for a ZPG 2DTBL for $Re_\theta = 1000$; (*b*) u/U_0 at $x/\theta_0 = 300$ for $Re_{\theta_0} = 900$ with $W_S/U_0 = 2$; and (*c*) $p/\rho U_0^2$ at $x/\theta_0 = 300$ for $Re_{\theta_0} = 900$ with $W_S/U_0 = 2$. The data shown have been obtained with $L_{x,W_S} = 100\theta_0$.

in a 2DTBL, we see a discernible departure from the classical log law in Q_r away from the wall. The reason for the departure is due to the effect of a 3DTBL persisting in this region, in particular, for a larger W_S (i.e. the cross-flow (the distribution of $\overline{W}$ is not shown here) is still present away from the wall). On the other hand, there is rather quick recovery to a 2DTBL in the inner region. In this context, Bassina, Strelets & Spalart (2001) examined the performance of several eddy viscosity models, i.e. SA (Spalart & Allmaras 1994) and SST (Menter 1994) models, in the recovery region of the present flow. They noted that, while the eddy viscosity models cannot reproduce the significant deviation between the Reynolds stress and mean shear-stress vectors present in the recovery region, the agreement of the computations with the data on the mean flow characteristics is unexpectedly good. They pointed out that the inner layer has much control over the skin friction and does not contain protracted 3-D effects. This latter behaviour is consistent with that observed in the present DNS.

As for turbulence statistics, a large outer peak appears for k^+ (figure 24*c*) and p^+_{rms} (figure 24*d*) especially for a larger W_S, where the distribution of p^+_{rms} shows a larger

magnitude than that for a 2DTBL. Inspection of the instantaneous fields shows that vortical structures are energized in the outer layer compared with those in a 2DTBL (see figure 25). Also, whilst the negative region of the large-scale u structures is preferentially associated with vortical structures in the outer region of a 2DTBL (see figures 21*a* and 25*a*; also Adrian *et al*. 2000), both the positive and negative regions of the u structures tend to correlate with vortical structures in the outer layer of the recovery region (see figure 25*b*), which are also active in generating the Reynolds shear stress (the instantaneous product uv is not shown here). This latter behaviour is intrinsically linked to the increased outer peaks of k^+ (figure 24*c*) and τ^+ (not shown here) in the recovery region, which indicates that the recovery to the ZPG TBL state is slow due to the effect of three-dimensionality. Also, wall-attached structures with a size of δ_{99} are observed for the pressure fluctuation p (see figure 25*c*), which are not only inclined in the z direction but also become energetic due to the effect of three-dimensionality. This behaviour is consistent with the significant increase in p^+_{rms} in the recovery region (see figure 24*d*).

We also note that, in the outer region of the recovery region, the magnitude of the mixing length ℓ_m/δ_{99} is smaller than the value of a 2DTBL (i.e. $\ell_m/\delta_{99} \approx 0.1$) (see figure 24*b*). The magnitude of a_1 is also smaller than those for a 2DTBL (not shown here) since the Reynolds normal stress is more enhanced by the effect of three-dimensionality than the Reynolds shear stress (see the large outer peak in the distribution of k^+ shown in figure 24*c*). A similar trend is observed in the experiment of Antonia & Luxton (1972) on the sudden change of the surface condition (i.e. a rough to smooth wall surface), while the data of Antonia & Luxton (1972) show a much larger decrease than the present DNS data. The difference between the present study and that of Antonia & Luxton (1972) is most likely because the effect of a rough wall diffuses more significantly into the outer region than that of inviscid skewing. These results underline that the effect of three-dimensionality persists in the recovery region.

6. Conclusions

In the present study, we have performed a series of DNS of a shear-driven non-equilibrium 3DTBL over a flat plate. The present DNS set-up is analogous to the spinning cylinder experiment (Lohmann 1976; Driver & Hebbar 1987; Driver & Johnston 1990) but without a curvature effect. In the DNS, three values of the inlet momentum thickness Reynolds number Re_{θ_0} (300, 600 and 900) are used with several values of W_S. The present largest W_S/U_0 ($=2$) is comparable to the value ($=2.2$) of the spinning cylinder experiment by Lohmann (1976). Particular attention has been given to the effects of cross-flow and Reynolds number on the mean flow statistics and Reynolds stress in a non-equilibrium 3DTBL. The main conclusions are summarized as follows.

After imposing W_S, the mean streamwise vorticity $\overline{\Omega}_x$ increasingly propagates towards the outer region where there is a deficit of the mean streamwise velocity $\overline{U}$. The mean streamwise velocity deficit is shown to be essentially due to inviscid skewing (i.e. three-dimensionality) (see relations (1.5) and (1.6)). The increase in the value of L_{x,W_S} (i.e. the streamwise extent of imposing W_S) leads to the further propagation of $\overline{\Omega}_x$ downstream of a 3DTBL. The approach to the collateral state is, however, slow in the present 3DTBL especially for $\overline{U}$.

In the present 3DTBL, near-plateaus are obtained in the skin friction coefficients, as in the experiment of Lohmann (1976). Indeed, the magnitudes of the plateaus increase with increasing W_S, while showing a departure from the collateral state. Inspection of the mean energy balance has revealed that, even when $W_S/U_0 = 1$ (i.e. $\tan^{-1}(W_S/U_0) = -45^\circ$ and

$-\overline{uv} \approx \overline{vw}$ is thus expected), the primary Reynolds shear stress $\overline{uv}$ extracts energy from the mean flow less efficiently than the secondary Reynolds shear stress $\overline{vw}$. The increase in W_S yields a smaller extraction of the energy from the work done by $\overline{uv}$, while the $\overline{vw}$ contribution to the skin friction increases with increasing W_S. The near-wall Reynolds stresses, normalized by U_0^2, also increase with cross-flow due to the increased straining. This behaviour corroborates the PIV measurement by Kiesow & Plesniak (2003). Also, near-wall vortical structures become intensified with increasing W_S, essentially associated with the increased skin friction coefficients. When the normalization is made with inner variables, the magnitude of $\overline{ww}/U_\tau^2$ exceeds that of $\overline{uu}/U_\tau^2$ when $W_S/U_0 \geq 1$. The inter-component energy transfer (pressure strain) is indeed changed, *viz.* the energy is transferred from the w component to the u component.

As the Reynolds number increases, the streamwise locations at which both $C_{f,x}$ and $C_{f,z}$ attain near-plateaus become smaller in terms of x/θ_0. The streamwise extent for obtaining a plateau in $C_{f,x}$ is $150\theta_0$, $165\theta_0$ and $40\theta_0$ (or, equivalently, $18\delta_0$, $8\delta_0$ and $5\delta_0$) for $Re_{\theta_0} = 300$, 600 and 900, respectively. The streamwise extent for $Re_{\theta_0} = 900$ (i.e. $5\delta_0$ or $40\theta_0$) is approximately a half that of Lohmann (1976) in this spinning cylinder experiment. The reason for the difference is likely to be because the imposition of W_S yields a 3DTBL more efficiently over a flat plate than over a spinning cylinder. When near-plateaus are obtained for the skin friction coefficients in a 3DTBL, the present structure parameter a_1 becomes identical with that in the inner region ($y/\delta_{99} \leq 0.2$) of an equilibrium 3DTBL. The largest magnitude of a_1 ($=0.14$) comparable to that for a 2DTBL is attained at the y location where the deficits of $\bar{U}$ and $\partial\overline{W}/\partial x > 0$ are the largest. The present results indicate that the plateau is an indicator, not for the collateral state, but for a state with a constant flow angle in the near-wall region. On the other hand, the mean velocity magnitude Q_r exhibits a discernible departure from the classical log law at a downstream station of a non-equilibrium 3DTBL (i.e. a larger von Kármán constant $\kappa = 0.44$ than in a 2DTBL). At the largest Re_{θ_0} ($=900$) with a large magnitude of cross-flow (i.e. $W_S/U_0 = 2$), the energy equilibrium ($P_k \simeq \bar{\varepsilon}$) and constant shear stress ($\tau \simeq \rho U_\tau^2$) assumptions are satisfied approximately; the overlap scaling is established unambiguously for $\bar{\varepsilon}$ but with a large value of $\kappa_\varepsilon = 0.44$, the latter value being larger than $\kappa_\varepsilon = 0.39$ in a 2DTBL (Abe & Antonia 2016). This indicates a better self-similar behaviour for small scales than for large scales. As for a 2-D flow (see the DNS works in a turbulent channel flow by Abe & Antonia 2016, 2017), small scales are likely to lose the Re dependence more rapidly than large scales in the present 3DTBL.

The instantaneous fields highlight the presence of asymmetric turbulence structures (i.e. toppling structures) due to cross-flow in the present 3DTBL where the negative u structures preferentially correlate with vortical structures (see figure 17). In the outer region, the large-scale u structures exhibit a less anisotropic behaviour with increasing W_S than those in a 2DTBL (see figure 21). Inspection of the spanwise u spectra below $y/\delta_{99} = 0.2$ has revealed that the most energetic length scale increases linearly with distance from the wall y, which indicates a self-similar behaviour in the toppling u structure. This latter finding supports the self-similar response of a non-equilibrium 3DTBL recently reported by Lozano-Durán *et al.* (2020) in a temporally developing 3-D channel DNS.

We also note that there is a significantly decreased magnitude of the primary Reynolds shear stress $\overline{uv}$ and thus a_1 in the present 3DTBL, which is commonly observed in 3DTBLs (see Eaton 1995). The reason for the reduction in the present flow is due to the reduced interaction between the inner and outer regions by inviscid skewing (i.e. three-dimensionality). The latter is intrinsically associated with the reduced $C_{f,x}$ (see the spectral analysis in § 5.3). Note that the reduction in $\overline{uv}$ observed in the present study

is most likely identical with that recently reported by Lozano-Durán *et al.* (2020) in the 3-D channel DNS since, in both 3DTBLs, the mean streamwise vorticity $\overline{\Omega}_x$ propagates towards the outer region (see § 3.2), and mean spanwise shear yields a self-similar behaviour (see § 5.3). The decreased $\overline{uv}$ is also associated with the lag between the mean strain and Reynolds shear-stress vectors and thus the anisotropy in the turbulent eddy viscosity. Indeed, the anisotropy of the turbulent eddy viscosity is observed in a near-equilibrium 3DTBL where Rotta's (1979) T model reproduces $\overline{uv}$ reasonably with $T = 0.9$.

After turning off W_S, there is again a sudden change of the surface condition (i.e. from 3-D to 2-D). Whilst the near-wall region adjusts to a new boundary condition rather quickly, there appears a large departure from a 2DTBL in the outer region since the effect of three-dimensionality persists there. In particular, the Reynolds normal stress is more enhanced than the Reynolds shear stress (see the large outer peak in the distributions of k^+ and p^+_{rms} shown in figure 24*c*,*d*), yielding a smaller magnitude of the mixing length scale (i.e. ℓ_m/δ_{99}) than in a 2DTBL (see figure 24*b*). These behaviours are qualitatively similar to those observed in the experiment of Antonia & Luxton (1972) on the response of a TBL to a step change of the surface condition. In both flows, the perturbations are generated in a near-wall region and then diffuse outwards on moving downstream.

The present shear-driven 3DTBL DNS convincingly showed the propagation of the mean streamwise vorticity $\overline{\Omega}_x$ into the outer region. The effect of inviscid skewing (i.e. three-dimensionality) is indeed significant. In particular, the approach to the collateral boundary layer is slow for $\overline{U}$ since, in a non-equilibrium 3DTBL, the primary Reynolds shear stress $\overline{uv}$ extracts energy from the mean flow less efficiently than the secondary Reynolds shear stress $\overline{vw}$. Also, the cross-flow affects the turbulence significantly, and yields a self-similar behaviour in the toppling u structures. These behaviours are major differences between the 2DTBL and non-equilibrium 3DTBL due to the three-dimensionality. The slow transition from 2DTBL to 3DTBL cannot be dismissed when modelling the present flow.

Acknowledgements

Computations performed on the JAXA (Japan Aerospace Exploration Agency) Supercomputer System are gratefully acknowledged. The author acknowledges discussions with Professors R. A. Antonia and L. Djenidi at the University of Newcastle, Professor I. Marusic at the University of Melbourne, Dr P. R. Spalart at the Boeing Commercial Airplane company and Dr G. Coleman at the NASA Langley Research Center. The author would also like to thank all three referees for their useful comments. This work was partially supported by JSPS KAKENHI grant no. 19K04207.

Declaration of interests

The author reports no conflict of interest.

REFERENCES

ABE, H. 2017 Reynolds-number dependence of wall-pressure fluctuations in a pressure-induced turbulent separation bubble. *J. Fluid Mech.* **833**, 563–598.

ABE, H. 2018 Direct numerical simulation of a shear driven three-dimensional turbulent boundary layer. In *Bulletin of the American Physical Society 71st Annual Meeting of the APS Division of Fluid Dynamics, Atlanta, GA*, November 18–20, vol. 63 (13), p. 281.

ABE, H. 2019 Direct numerical simulation of a turbulent boundary layer with separation and reattachment over a range of Reynolds numbers. *Fluid Dyn. Res.* **51**, 011409.

ABE, H. & ANTONIA, R. A. 2016 Relationship between the energy dissipation function and the skin friction law in a turbulent channel flow. *J. Fluid Mech.* **798**, 140–164.

ABE, H. & ANTONIA, R. A. 2017 Relationship between the heat transfer law and the scalar dissipation function in a turbulent channel flow. *J. Fluid Mech.* **830**, 300–325.

ABE, H., ANTONIA, R. A. & TOH, S. 2018 Large-scale structures in a turbulent channel flow with a minimal streamwise flow unit. *J. Fluid Mech.* **850**, 733–768.

ABE, H., KAWAMURA, H. & CHOI, H. 2004 Very large-scale structures and their effects on the wall shear-stress fluctuations in a turbulent channel flow up to $Re_\tau = 640$. *Trans. ASME J. Fluids Engng* **126**, 835–843.

ADRIAN, R. J., MEINHART, C. D. & TOMKINS, C. D. 2000 Vortex organization in the outer region of the turbulent boundary layer. *J. Fluid Mech.* **422**, 1–54.

AHN, J., LEE, J. H., LEE, J. L., KANG, J.-H. & SUNG, H. J. 2015 Direct numerical simulation of a 30R long turbulent pipe flow at $Re_\tau = 3008$. *Phys. Fluids* **27**, 065110.

ANDERSON, S. D. & EATON, J. K. 1989 Reynolds stress development in pressure-driven, three-dimensional, turbulent boundary layers. *J Fluid Mech.* **202**, 263–294.

ANTONIA, R. A. & LUXTON, R. E. 1971 The response of a turbulent boundary layer to an upstanding step change in surface roughness. *Trans. ASME: J. Basic Engng* **93**, 22–34.

ANTONIA, R. A. & LUXTON, R. E. 1972 The response of a turbulent boundary layer to a step change in surface roughness. Part 2. Rough-to-smooth. *J. Fluid Mech.* **53**, 737–757.

BALAKUMAR, B. J. & ADRIAN, R. J. 2007 Large- and very-large-scale motions in channel and boundary-layer flows. *Phil. Trans. R. Soc.* A **365**, 665–681.

BASSINA, I., STRELETS, M. & SPALART, P. R. 2001 Response of simple turbulence models to step changes of slip velocity. *AIAA J.* **39**, 201–210.

VAN DEN BERG, B., ELSENAAR, A., LINDHOUT, J. P. F. & WESSELING, P. 1975 Measurements in an incompressible three-dimensional turbulent boundary layer, under infinite swept-wing conditions, and comparison with theory. *J. Fluid Mech.* **70**, 127–148.

BISSONNETTE, L. R. & MELLOR, G. L. 1974 Experiments on the behaviour of an axisymmetric turbulent boundary layer with a sudden circumferential strain. *J. Fluid Mech.* **63**, 369–413.

BRADSHAW, P. 1987 Turbulent secondary flows. *Annu. Rev. Fluid Mech.* **19**, 53–74.

BRADSHAW, P. & PONTIKOS, N. S. 1985 Measurements in the turbulent boundary layer on an 'infinite' swept wing. *J. Fluid Mech.* **159**, 105–130.

COLEMAN, G. N., KIM, J. & LE, A.-T. 1996 A numerical study of three-dimensional wall-bounded flows. *Intl J. Heat Fluid Flow* **17**, 333–342.

COLEMAN, G. N., KIM, J. & SPALART, P. R. 2000 A numerical study of strained three-dimensional wall-bounded turbulence. *J. Fluid Mech.* **416**, 75–116.

COLEMAN, G. N., RUMSEY, C. L. & SPALART, P. R. 2019 Numerical study of a turbulent separation bubble with sweep. *J. Fluid Mech.* **880**, 684–706.

DECK, S., RENARD, N., LARAUFIE, R. & WEISS, P.-E. 2014 Large-scale contribution to mean wall shear stress in high-Reynolds-number flat-plate boundary layers up to $Re_\theta = 13650$. *J. Fluid Mech.* **743**, 202–248.

DRIVER, D. M. & HEBBAR, S. K. 1987 Experimental study of a three-dimensional, shear-driven, turbulent boundary layer. *AIAA J.* **25**, 35–42.

DRIVER, D. M. & JOHNSTON, J. P. 1990 Experimental study of a three-dimensional shear-driven turbulent boundary layer with streamwise adverse pressure gradient. *NASA TM* 102211.

EATON, J. K. 1995 Effects of mean flow three dimensionality on turbulent boundary-layer structure. *AIAA J.* **33**, 2020–2025.

FUKAGATA, K., IWAMOTO, K. & KASAGI, N. 2002 Contribution of Reynolds stress distribution to the skin friction in wall-bounded flows. *Phys. Fluids* **14** (11), 73–76.

FURUYA, Y., NAKAMURA, I. & KAWACHI, H. 1966 The experiment on the skewed boundary layer on a rotating body. *Bull. JSME* **9** (36), 702–710.

GUALA, M., HOMMEMA, S. E. & ADRIAN, R. J. 2006 Large-scale and very-large-scale motions in turbulent pipe flow. *J. Fluid Mech.* **554**, 521–542.

GUNGOR, A. G., MACIEL, Y., SIMENS, M. & SORIA, J. 2014 Analysis of a turbulent boundary layer subjected to a strong adverse pressure gradient. *J. Phys.: Conf. Ser.* **506**, 012007.

HOYAS, S. & JIMÉNEZ, J. 2008 Reynolds number effects on the Reynolds-stress budgets in turbulent channels. *Phys. Fluids* **20**, 101511.

HUTCHINS, N. & MARUSIC, I. 2007 Evidence of very long meandering features in the logarithmic region of turbulent boundary layers. *J. Fluid Mech.* **579**, 467–477.

HWANG, Y. 2015 Statistical structure of self-sustaining attached eddies in turbulent channel flow. *J. Fluid Mech.* **767**, 254–289.

JIMÉNEZ, J. & HOYAS, S. 2008 Turbulent fluctuations above the buffer layer of wall-bounded flows. *J. Fluid Mech.* **611**, 215–236.

JOHNSTON, J. P. 1960 On the three-dimensional turbulent boundary layer generated by secondary flow. *Trans. ASME: J. Basic Engng* **82**, 233–246.

JOHNSTON, J. P. & FLACK, K. A. 1996 Review – advances in three-dimensional turbulent boundary layers with emphasis on the wall-layer regions. *Trans. ASME: J. Fluids Engng* **118**, 219–232.

KANG, H. S., CHOI, H. & YOO, J. Y. 1998 On the modification of the near-wall coherent structure in a three-dimensional turbulent boundary layer on a free rotating disk. *Phys. Fluids* **10**, 2315–2322.

KANNEPALLI, C. & PIOMELLI, U. 2000 Large-eddy simulation of a three-dimensional shear-driven turbulent boundary layer. *J. Fluid Mech.* **423**, 175–203.

KEVIN, K., MONTY, J. & HUTCHINS, N. 2019 Turbulent structures in a statistically three-dimensional boundary layer. *J. Fluid Mech.* **859**, 543–565.

KIESOW, R. O. & PLESNIAK, M. W. 2003 Near-wall physics of a shear-driven three-dimensional turbulent boundary layer with varying crossflow. *J. Fluid Mech.* **484**, 1–39.

KONG, H., CHOI, H. & LEE, J. S. 2000 Direct numerical simulation of turbulent thermal boundary layers. *Phys. Fluids* **12**, 2555–2568.

LITTELL, H. & EATON, J. 1994 Turbulence characteristics of the boundary layer on a rotating disk. *J. Fluid Mech.* **266**, 175–207.

LOHMANN, R. P. 1976 Response of a developed turbulent boundary layer to local transverse surface motion. *Trans. ASME: J. Fluids Engng* **98**, 354–363.

LOZANO-DURÁN, A., GIOMETTO, M. G., PARK, G. I. & MOIN, P. 2020 Non-equilibrium three-dimensional boundary layers at moderate Reynolds numbers. *J. Fluid Mech.* **833**, A20.

LUND, T. S., WU, X. & SQUIRES, K. D. 1998 Generation of turbulent inflow data for spatially-developing boundary layer simulation. *J. Comput. Phys.* **140**, 233–258.

MARUSIC, I., MONTY, J. P., HULTMARK, M. & SMITS, A. J. 2013 On the logarithmic region in wall turbulence. *J. Fluid Mech.* **716**, R3.

MENTER, F. R. 1994 Two-equation eddy-viscosity turbulence models for engineering applications. *AIAA J.* **32** (8), 1598–1605.

MCLEAN, D. J. 2013 *Understanding Aerodynamics – Arguing from the Real Physics*. Wiley.

MOIN, P., SHIH, T. H., DRIVER, D. & MANSOUR, N. N. 1990 Direct numerical simulation of a three-dimensional turbulent boundary layer. *Phys. Fluids* A **2**, 1846–1853.

MORINISHI, Y., LUND, T. S., VASILYEV, O. V. & MOIN, P. 1998 Fully conservative higher order finite difference schemes for incompressible flow. *J. Comput. Phys.* **143**, 90–124.

NICKELS, T. B., MARUSIC, I., HAFEZ, S., HUTCHINS, N. & CHONG, M. S. 2007 Some predictions of the attached eddy model for a high Reynolds number boundary layer. *Phil. Trans. R. Soc.* A **365**, 807–822.

ÓĘLCMEN, S. M. & SIMPSON, R. L. 1993 Evaluation of algebraic eddy-viscosity models in three-dimensional turbulent boundary layer flows. *AIAA J.* **31**, 1545–1554.

ÓĘLCMEN, S. M. & SIMPSON, R. L. 1995 An experimental study of a three-dimensional pressure-driven turbulent boundary layer. *J. Fluid Mech.* **290**, 225–262.

PIERCE, F. J. & MCALLISTER, J. E. 1983 Near-wall similarity in a shear-driven three-dimensional turbulent boundary layer. *Trans. ASME: J. Fluids Engng* **105**, 263–269.

RENARD, N. & DECK, S. 2016 A theoretical decomposition of mean skin friction generation into physical phenomena across the boundary layer. *J. Fluid Mech.* **790**, 339–367.

ROTTA, J. C. 1962 Turbulent boundary layers in incompressible flow. *Prog. Aeronaut. Sci.* **2**, 1–219.

ROTTA, J. C. 1979 A family of turbulence models for three-dimensional boundary layers. In *Turbulent Shear Flows I* (ed. F. Durst, B. E. Launder, F. W. Schmidt & J. H. Whitelaw), pp. 267–278. Springer.

SCHLATTER, P. & BRANDT, L. 2010 DNS of spatially-developing three-dimensional boundary layers. In *Direct and Large-Eddy Simulation VII* (ed. V. Armenio, B. Geurts & J. Fröhlich), pp. 57–63. Springer.

SCHLATTER, P. & ÖRLÜ, R. 2010 Assessment of direct numerical simulation data of turbulent boundary layers. *J. Fluid Mech.* **659**, 116–126.

SENDSTAD, O. & MOIN, P. 1992 The near wall mechanics of three-dimensional turbulent boundary layers. *Rep.* TF-57. Thermosciences Division, Department of Mechanical Engineering, Stanford University.

SIMENS, M. P., JIMENEZ, J., HOYAS, S. & MIZUNO, Y. 2009 A high-resolution code for turbulent boundary layers. *J. Comput. Phys.* **228**, 4218–4231.

SMITS, A. J., MATHESON, N. & JOUBERT, P. N. 1983 Low-Reynolds-number turbulent boundary layers in zero and favourable pressure gradients. *J. Ship Res.* **27**, 147–157.

SPALART, P. R. 1988 Direct simulation of a turbulent boundary layer up to $R_\theta = 1410$. *J. Fluid Mech.* **187**, 61–98.

SPALART, P. R. 1989 Theoretical and numerical study of a three-dimensional turbulent boundary layer. *J. Fluid Mech.* **205**, 319–340.

SPALART, P. R. & ALLMARAS, S. R. 1994 A one-equation turbulence model for aerodynamic flows. *Rech. Aerosp.* **1**, 5–21.

SPALART, P. R. & STRELETS, M. 2000 Mechanisms of transition and heat transfer in a separation bubble. *J. Fluid Mech.* **403**, 329–349.

SPALART, P. R., STRELETS, M. & TRAVIN, A. 2006 Direct numerical simulation of large-eddy-break-up devices in a boundary layer. *Int. J. Heat Fluid Flow* **27**, 902–910.

SPALART, P. R. & WATMUFF, J. H. 1993 Experimental and numerical study of a turbulent boundary layer with pressure gradients. *J. Fluid Mech.* **249**, 337–371.

TOMKINS, C. D. & ADRIAN, R. J. 2005 Energetic spanwise modes in the logarithmic layer of a turbulent boundary layer. *J. Fluid Mech.* **545**, 141–162.

TOWNSEND, A. A. 1976 *The Structure of Turbulent Shear Flow*, vol. 2. Cambridge University Press.

WEI, T. 2018 Integral properties of turbulent-kinetic-energy production and dissipation in turbulent wall-bounded flows. *J. Fluid Mech.* **854**, 449–473.

WHITE, F. M. 1991 *Viscous Fluid Flow*, 3rd edn. McGraw-Hill.

WU, X. & MOIN, P. 2009 Direct numerical simulation of turbulence in a nominally-zero-pressure-gradient flat-plate boundary layer. *J. Fluid Mech.* **630**, 5–41.

WU, X. & SQUIRES, K. D. 1997 Large eddy simulation of an equilibrium three-dimensional turbulent boundary layer. *AIAA J.* **35**, 67–74.